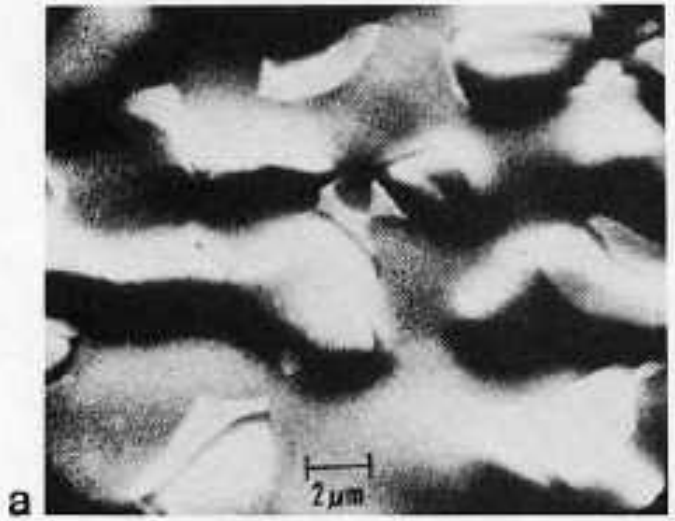

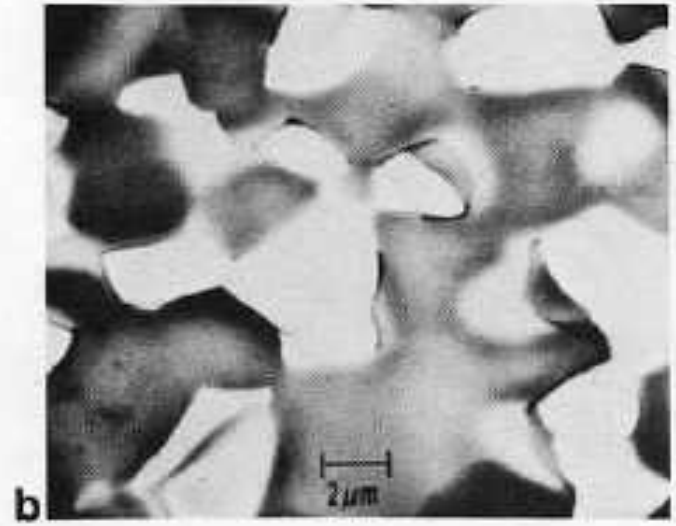

Figure 4.39. Separation of contrast components with emissive mode and specimen-current mode images. The specimen is eutectic lead–tin alloy, which has two phases, with surface topography in the form of ripples due to polishing. (a) Negatively biased E–T detector; the detector is located at the top of the image. (b) Specimen-current, contrast reversed so that the phase with the higher average atomic number appears bright.

Figure 4.48. Schematic illustration of a line-trace display of a signal with characteristics that can produce a good image for an observer. The image is perceived as filling out the dynamic range of the display, from near full black to near full white, with no saturation.

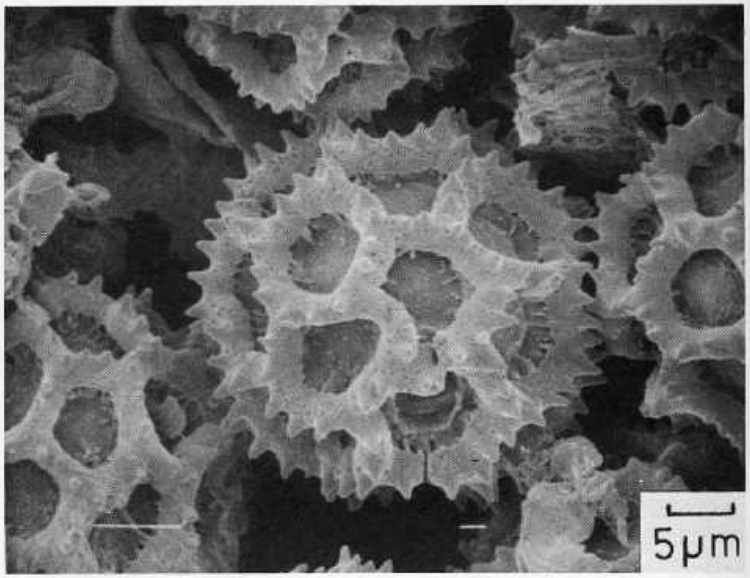

Figure 4.49. Example of linear amplification applied to a sample which produces high natural contrast by the topographic contrast mechanism. Positively biased E–T detector. (Specimen: pollen grains; courtesy JEOL.)

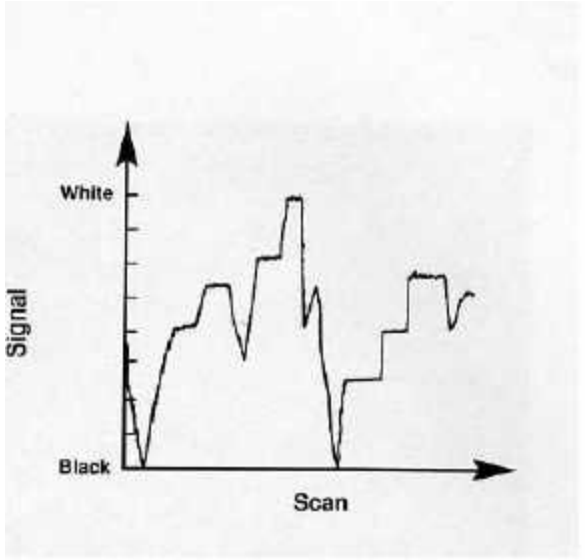

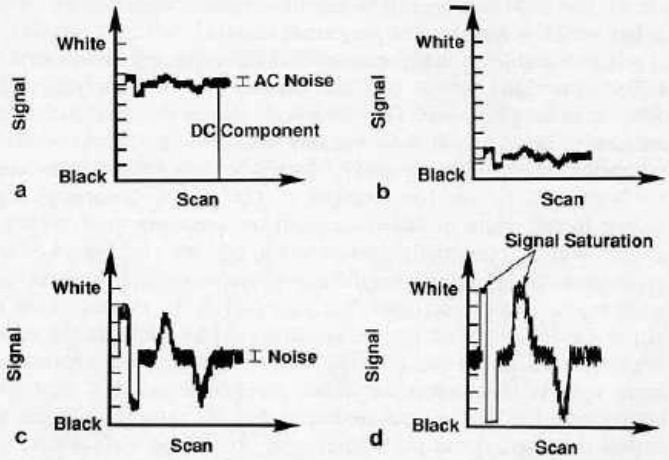

Figure 4.50. Schematic illustration of the steps required to apply differential amplification to enhance weak contrast in an image. (a) Line trace of a specimen which produces low natural contrast. The modulations of the signal (contrast) due to specimen features, confined to one or two gray levels, are poorly visible. (b) A constant (DC) level is subtracted from the signal at every point. (c) The difference signal is amplified, expanding the range of gray levels over which the specimen contrast is displayed. (d) Excessive application of differential amplification leads to signal saturation.

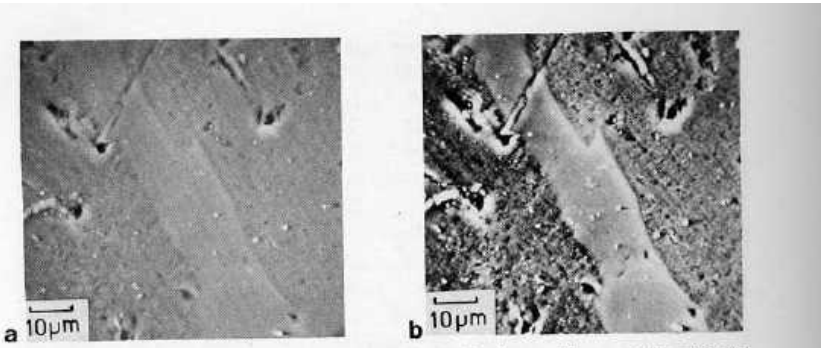

Figure 4.51. Weak atomic number contrast in an aluminum–silicon eutectic enhanced by differential amplification. (a) Natural contrast approximately 7% displayed with linear amplification. The brighter silicon band is barely visible against the darker surrounding aluminum. (b) Same image as (a), but with differential amplification applied. Note the bright areas of saturation around some of the voids in the specimen.

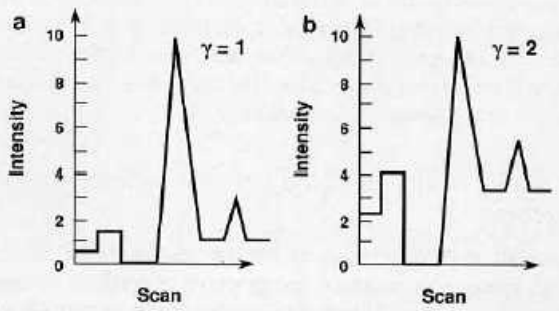

Figure 4.52. (a) Schematic illustration of a line trace for which the signal spans the full dynamic range of the display, but the information of interest lies in a narrow gray-scale range near the zero of signal (dark regions). (b) Same signal trace, but with nonlinear amplification applied ($\gamma = 2$).

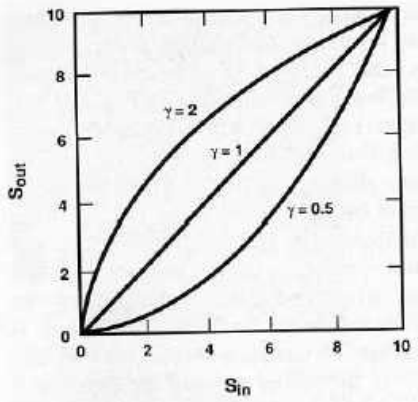

Figure 4.53. Signal response functions for nonlinear amplification (gamma processing). For $\gamma = 2$, the contrast at the dark end of the gray scale is expanded, improving the visibility of dark objects. For $\gamma = 0.5$, the expansion of contrast occurs at the bright end of the gray scale.

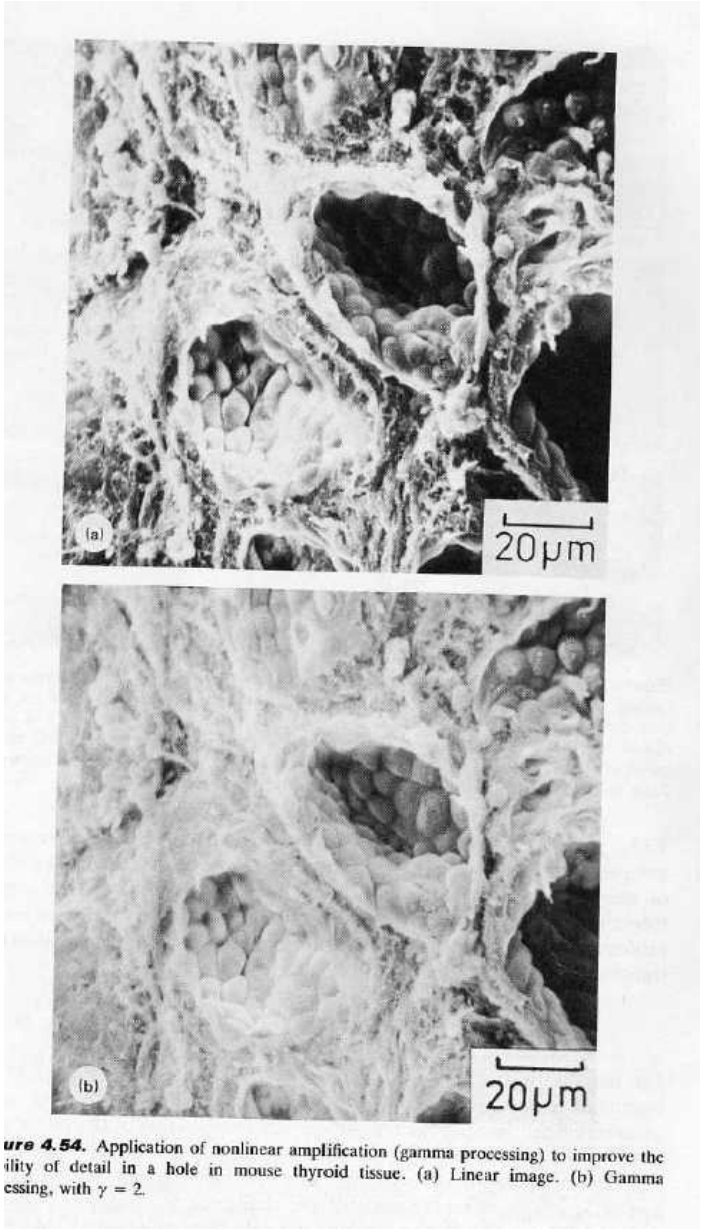

ure 4.54. Application of nonlinear amplification (gamma processing) to improve the ility of detail in a hole in mouse thyroid tissue. (a) Linear image. (b) Gamma essing, with $\gamma = 2$.

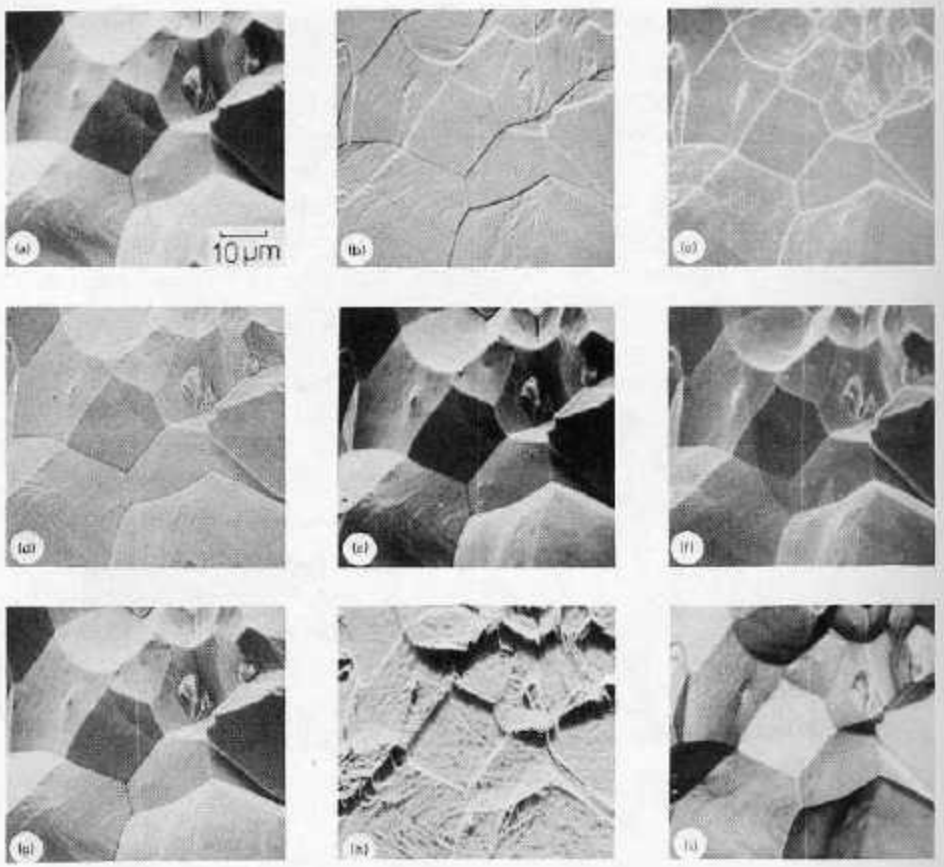

Figure 4.55. Images of an iron fracture surface with various types of signal processing applied: (a) direct + E–T image; (b) first time derivative; (c) absolute value of the first time derivative; (d) second time derivative; (e) 50% direct image plus 50% first time derivative; (f) 50% direct image plus 50% absolute first time derivative; (g) 50% direct image plus 50% second time derivative; (h) *Y*-modulation image; (i) reversed contrast. Beam energy 20 keV.

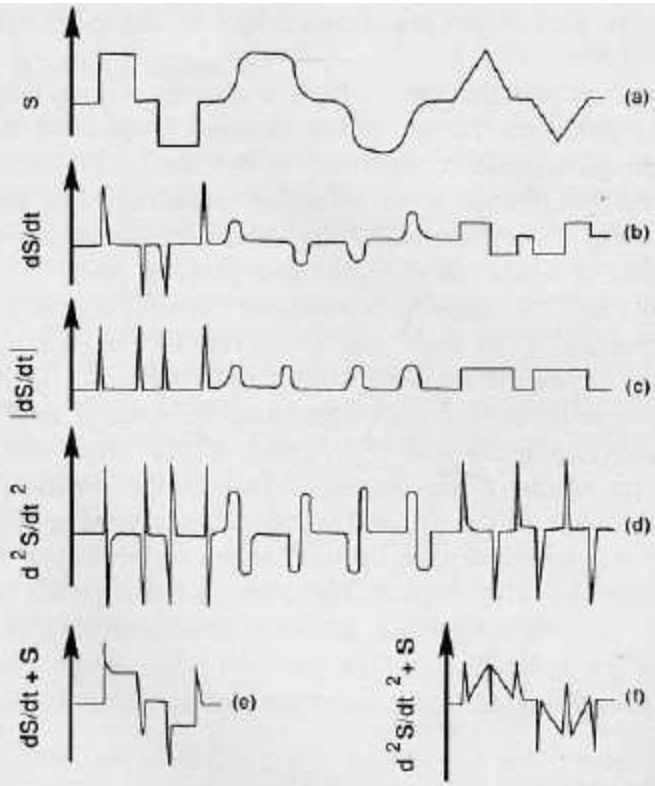

Figure 4.56. Signal traces of time-derivative processing operations: (a) direct signal; (b) first time derivative; (c) absolute value of the first derivative; (d) second derivative; (e) signal mixing, direct signal plus first derivative; (f) signal mixing, direct signal plus second derivative.

RESOLUTION

Beam Size : Aberrations, Working Distance

Type of Signal : Back Scattered, Secondary
X-ray

Beam Spreading : Voltage, Atomic No. (Z)

Contrast : Specimen, Beam Current

↓ ↓

Z, Topography Voltage Current

Limit of diffraction = $0.61\ \lambda/2$

$d_{sperical} = 0.68\ \ C_s^{1/4} \lambda^{3/4}$

$d_{chromatic} = 1.1\ \ \lambda^{1/2} (C_c \delta E/E)^{1/2}$

$$d_{total}^2 = \sum_i d_i^2$$

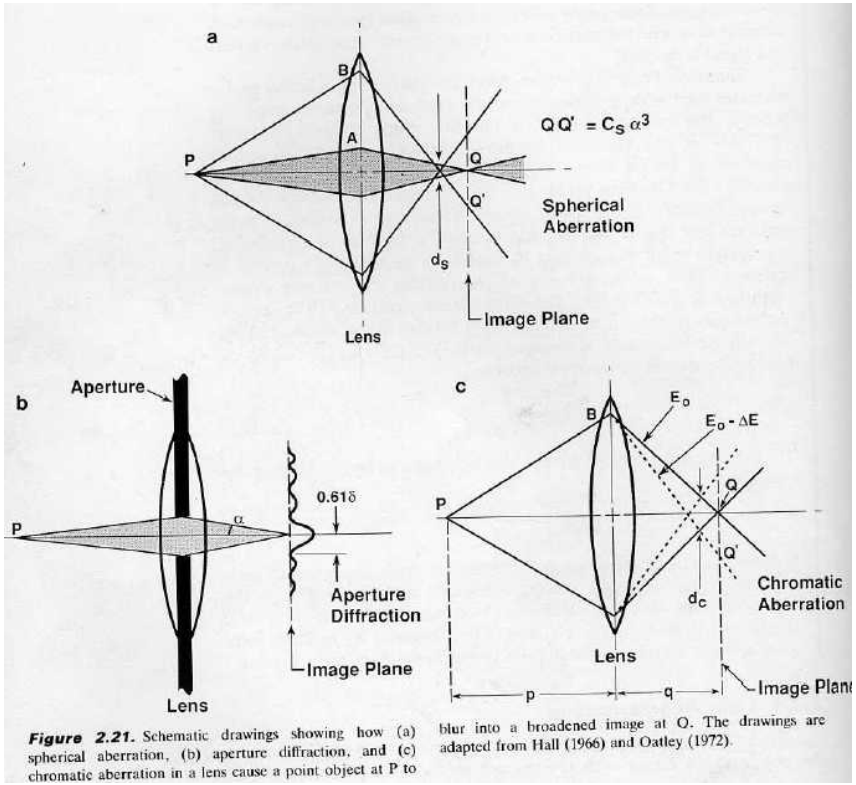

Figure 2.21. Schematic drawings showing how (a) spherical aberration, (b) aperture diffraction, and (c) chromatic aberration in a lens cause a point object at P to blur into a broadened image at Q. The drawings are adapted from Hall (1966) and Oatley (1972).

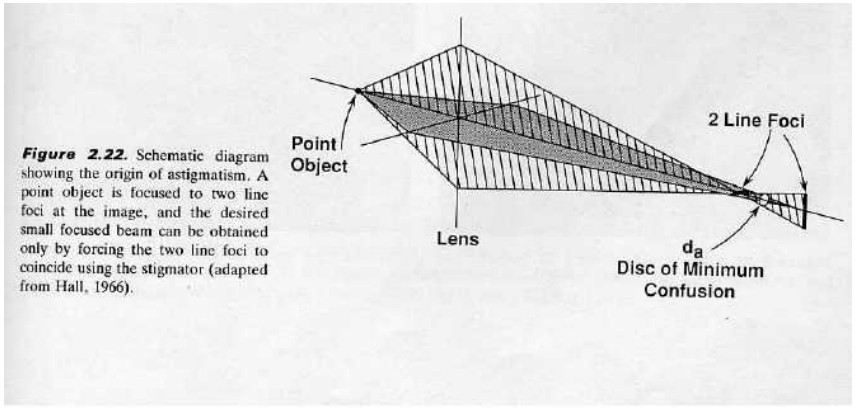

Figure 2.22. Schematic diagram showing the origin of astigmatism. A point object is focused to two line foci at the image, and the desired small focused beam can be obtained only by forcing the two line foci to coincide using the stigmator (adapted from Hall, 1966).

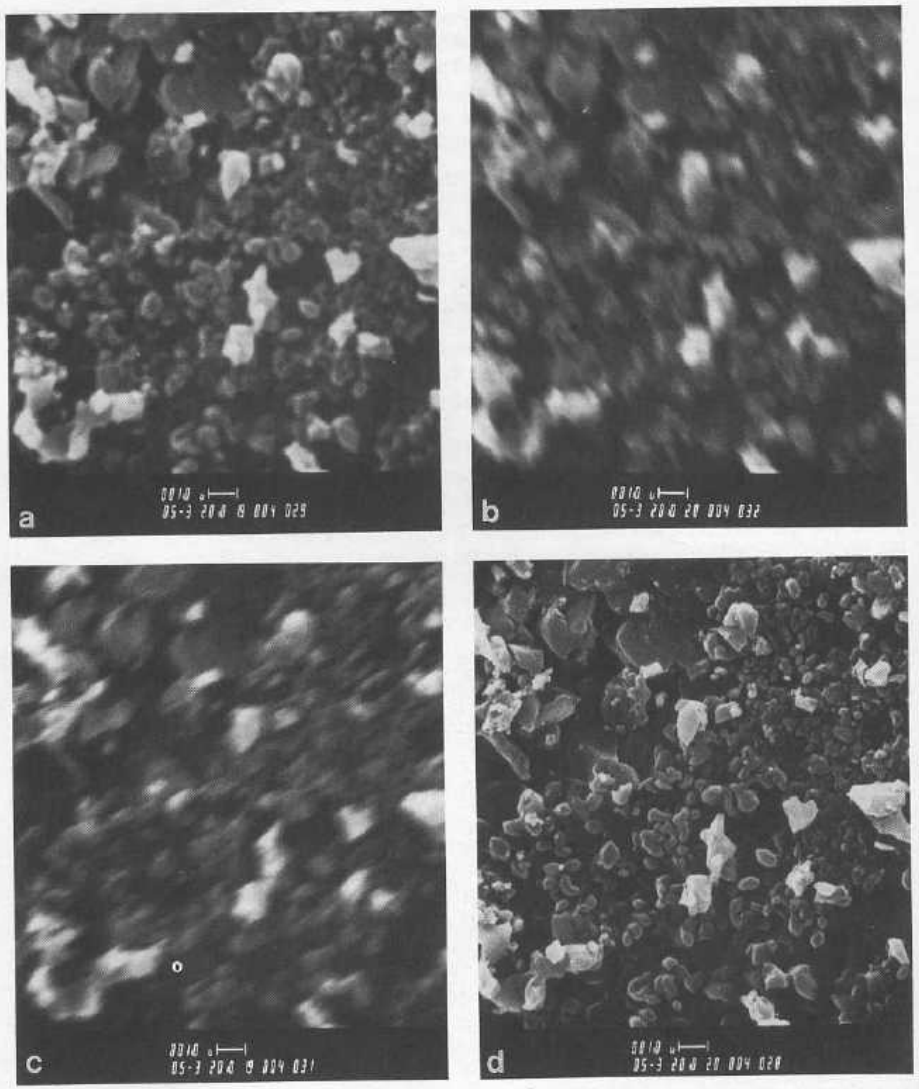

Figure 2.23. Effect of astigmatism in the probe-forming lens: (a) initial image before astigmatism correction, (b) underfocus, (c) overfocus, and (d) image corrected for astigmatism.

LIMITS ON PROBE SIZE AND APERTURES DUE TO ABERRATIONS AND DIFFRACTION

In general, $\mathbf{d^2_{tot} = P/\alpha^2 + Q\alpha^2 + R\alpha^6}$

$\mathbf{P = 4i_{beam}/\pi^2\beta + (0.61\lambda)^2}$ Finite Beam Size and Diffraction

$\mathbf{Q = (C_c\delta E/E)^2 + C^2_a}$ Chromatic

$\mathbf{R = (0.3C_s)^2}$ Spherical

Considering ONLY *spherical aberration* (with diffraction and beam current) one can derive minimum spot sizes for a particular beam current. This also specifies an *optimum aperture size*. Below this size you are *losing brightness with no benefit in resolution*. Above this size, you *lose resolution for that beam current.*

Similarly, one can derive optimal conditions when *ONLY chromatic aberration* is present.

At high beam currents, resolution is largely limited by spherical aberration. At low voltages and low beam currents, chromatic aberration becomes important. The above information is shown in figures 4.3 – 4.5 in the transparencies. *Note : i_0 is brightness, normalised by the accelerating voltage.*

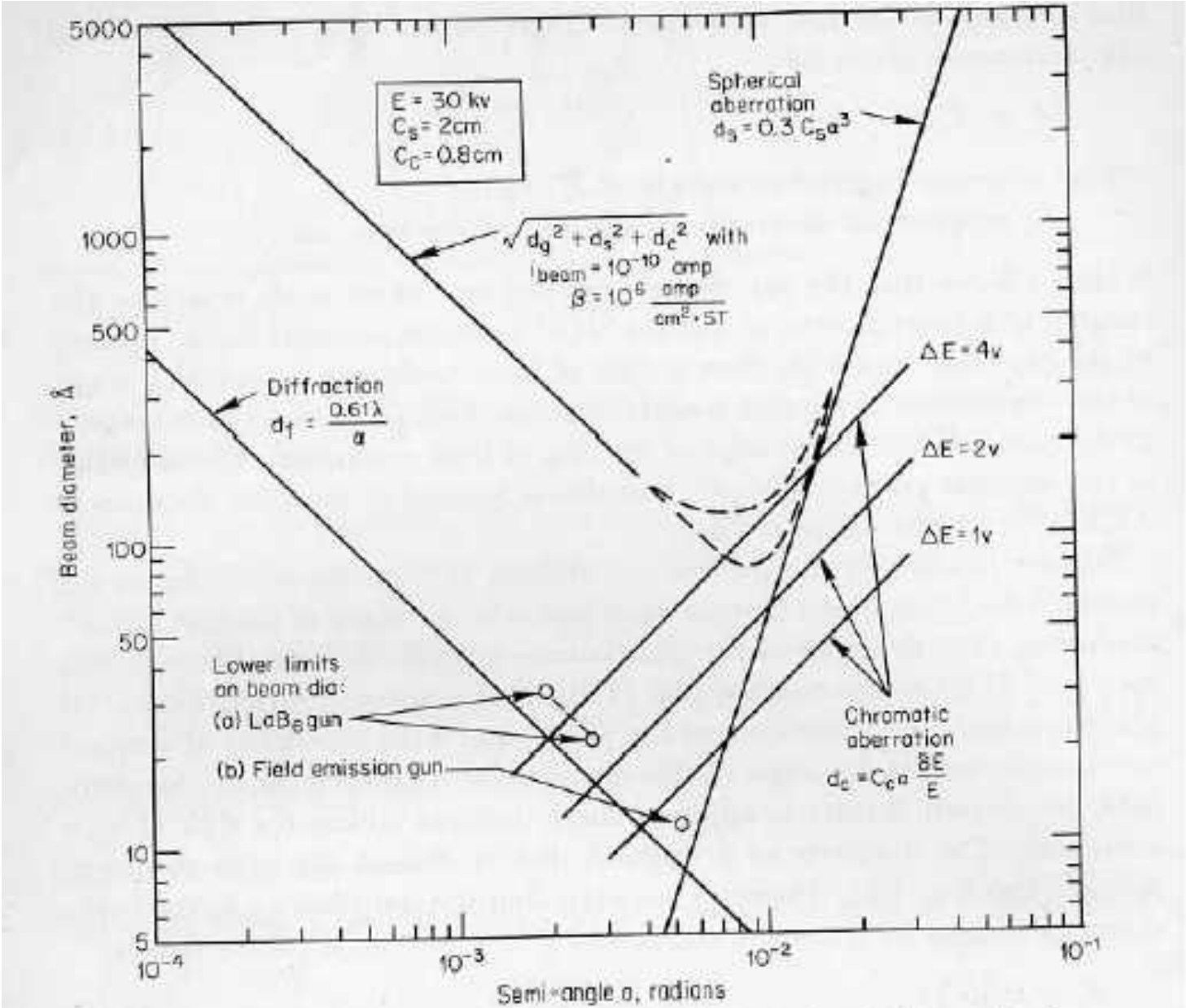

FIG. 4.3 Diffraction diameter d_f and aberration diameters d_c and d_s as a function of semiangle α.

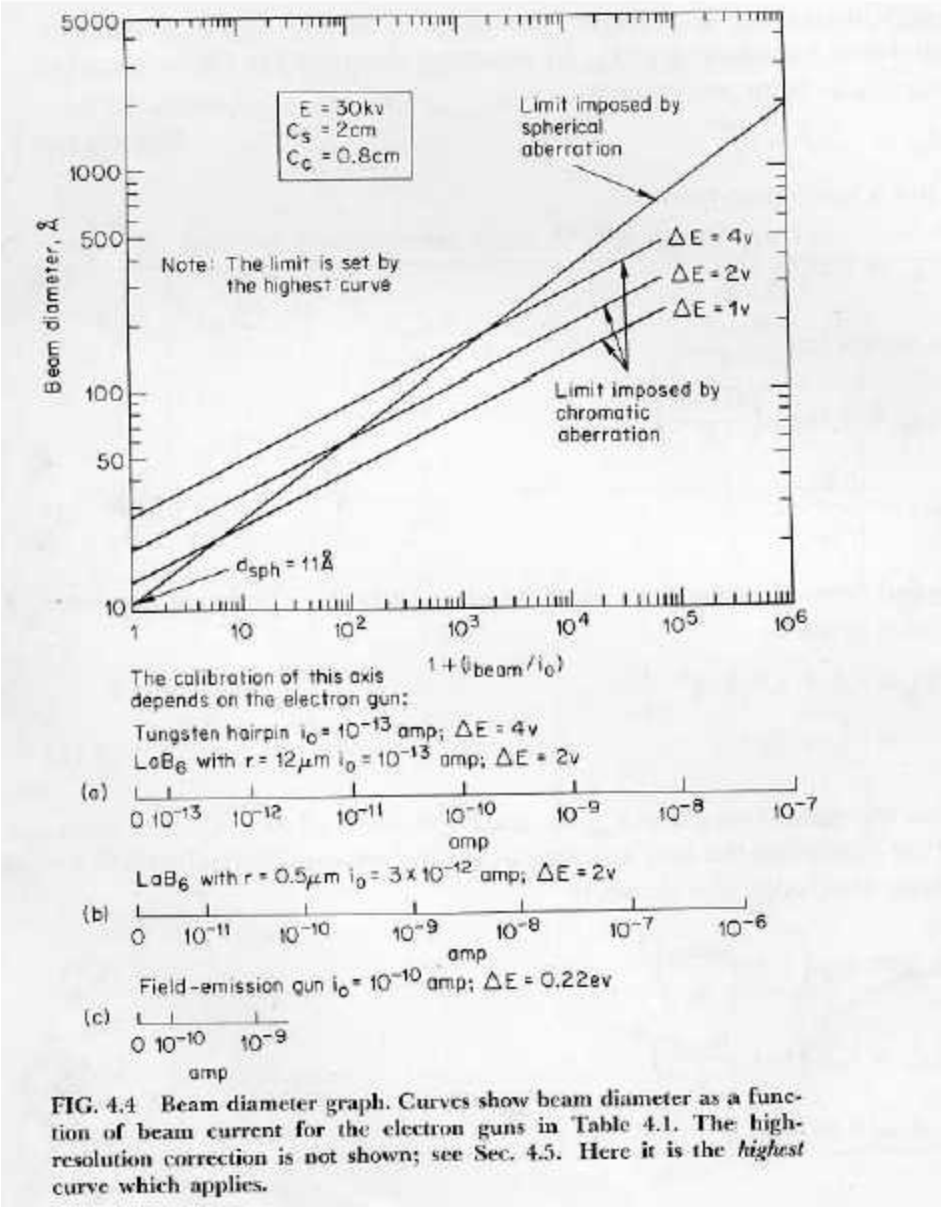

FIG. 4.4 Beam diameter graph. Curves show beam diameter as a function of beam current for the electron guns in Table 4.1. The high-resolution correction is not shown; see Sec. 4.5. Here it is the *highest* curve which applies.

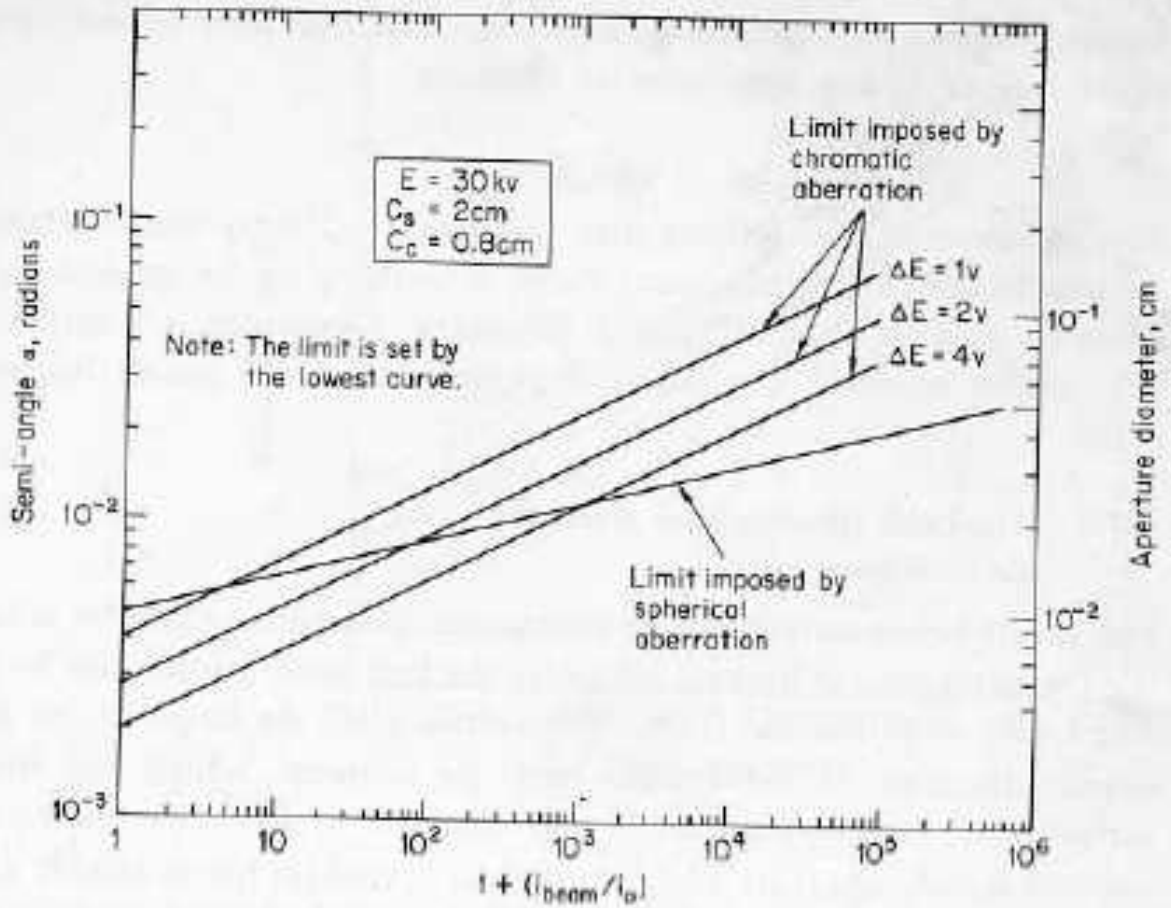

FIG. 4.5 Aperture size graph. Curves show the optimum beam aperture as a function of beam current. Here it is the *lowest* curve which applies.

TABLE 4.1 *Electron-gun data*

Gun	Lifetime, hr	Brightness β at 25 kv, amps/cm² sterad	i_0, amps (See Eq. 4.29)	Energy spread δE, ev
Tungsten hairpin	80	2.9×10^{5}[a]	1.2×10^{-14}	?
	40	4.8×10^{5}	1.9×10^{-14}	1.6[b]
	16	9×10^{4}	3.6×10^{-14}	2.0
	8	1.5×10^{5}	6.2×10^{-14}	3.0
LaB_6 with tip radius = 10 to 12 μm	300–500 at 10^{-5} torr[c]	$1–2 \times 10^{6}$[d]	1.1×10^{-13}	2–3[f]
LaB_6 with tip radius = 1 μm	50–100 at 10^{-6} torr[e]	$5–6 \times 10^{6}$	3.3×10^{-12}	2–3[f]
Tungsten field emission	See footnote *g*	2×10^{8}	1.1×10^{-10}	0.22[g]

[a] Scaled from theoretical figures from Haine and Cosslett (1961, p. 134).
[b] Estimated from Pfeiffer (1971).
[c] LaB_6 rod must be cleaned at intervals of 100 hr.
[d] Scaled from Broers (1969*a*).
[e] The high brightness is contained within narrow lobes which can be located with the help of scanning coils below the gun (Fig. 5.5).
[f] Data provided by A. N. Broers.
[g] After Crewe, Isaacson, and Johnson (1971). Field-emission points must be re-formed at intervals of approximately 1 hr.

Table 4.2. Size of Picture Element as a Function of Magnification[a]

Magnification	Edge of picture element
10X	10 μm
100X	1 μm
1,000X	0.1 μm (100 nm)
10,000X	0.01 μm (10 nm)
100,000X	1 nm

[a] 1000 × 1000 scan matrix; 10 cm × 10 cm display on CRT.

scan-control module). Table 4.2 shows the length of the picture element's edge as a function of magnification for the case of a high-resolution (1000 × 1000) image.

For a given choice of magnification, images are considered to be in sharpest focus if the signal measured when the beam is addressed to a given picture element comes only from that picture element. From Table 4.2, the picture element decreases to nanometers at high magnification. Overlap of information from adjacent picture elements must eventually occur as the magnification is increased, because of the finite size of the interaction volume. This overlap of pixel information is manifested as blurring in the image, as illustrated in Fig. 4.8.

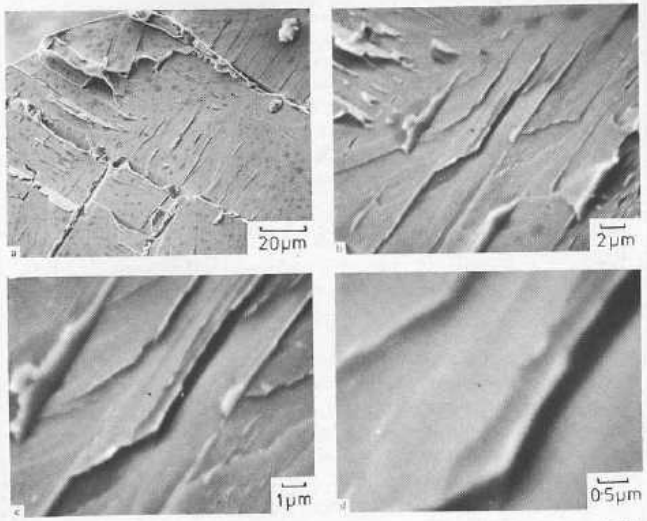

Figure 4.8. Images of a fracture surface illustrating the effects of pixel overlap (hollow magnification). The finest details in the image at low magnification appear sharp, while at the highest magnification, blurring can be observed.

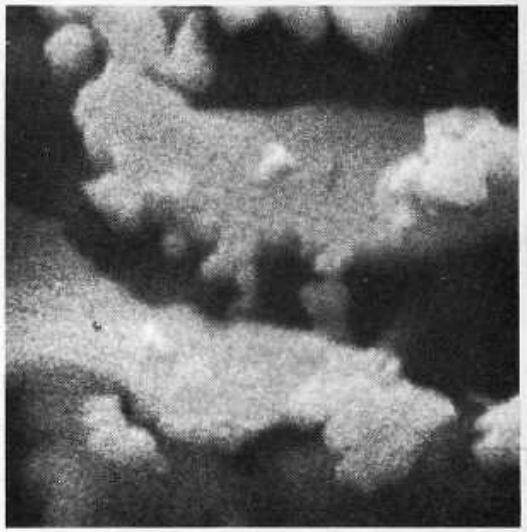

(a)

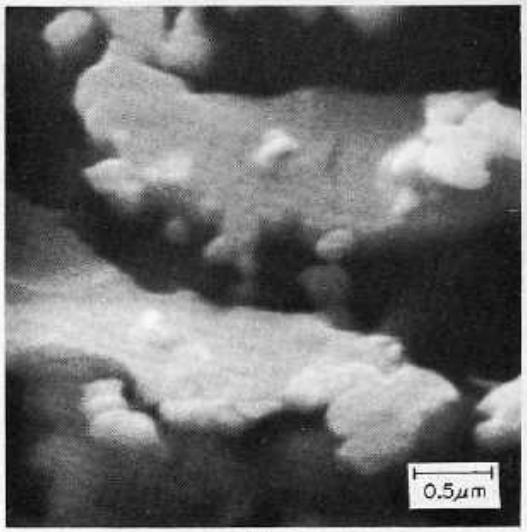

(b)

FIG. 2.1 Illustrating the effect of beam current and recording time on secondary electron image of silver mesh ($\theta = 30°$). (*a*) 3×10^{-12} amp, 40 sec, 20 kv; (*b*) 10^{-11} amp, 100 sec, 20 kv.

SIGNAL – NOISE, ETC.,

S = Signal, N = Noise,

$\Delta S > 5\ N$ to see anything

Contrast $C = \Delta S/S$

i_B = Beam Current must be greater than

(1000x1000 pixels) $\dfrac{4 \times 10^{-12}}{\in C^2 \tau_f}$ Ampere

$\in$ = detector efficiency

τ_f = time probe sits on one pixel

Low Contrast $\Rightarrow$ large i_B/Long τ_f

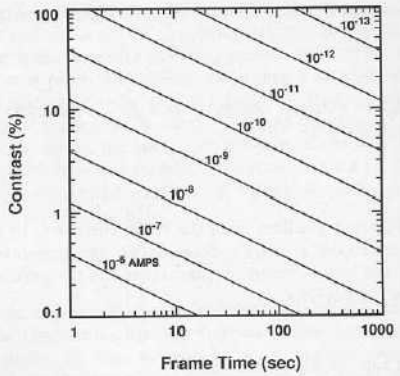

Figure 4.41. Graphical representation of the relationship of parameters of contrast, frame time, and beam current in the threshold equation. Assumptions: the signal production/collection efficiency $\varepsilon = 0.25$, and the scan is 1000 × 1000 picture elements.

Table 4.6. Gaussian Probe Size for Various Contrast Values (tungsten filament, 20 keV)

Contrast	d_{min} (nm)	Contrast	d_{min} (nm)
1.0	2.3	0.025	91
0.5	4.6	0.01	230
0.25	9.1	0.005	460
0.10	23	0.0025	911
0.05	46	0.001	2,300

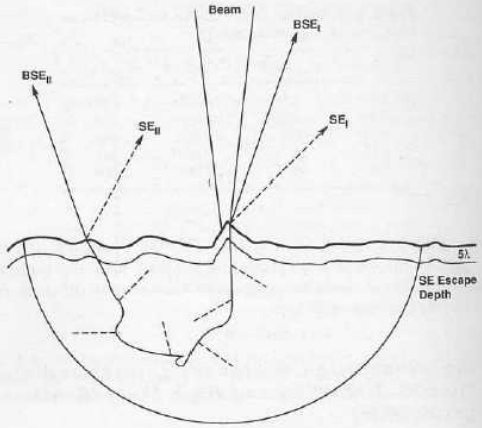

Figure 4.42. Backscattered- and secondary-electron signals emitted with a finely focused high-resolution beam.

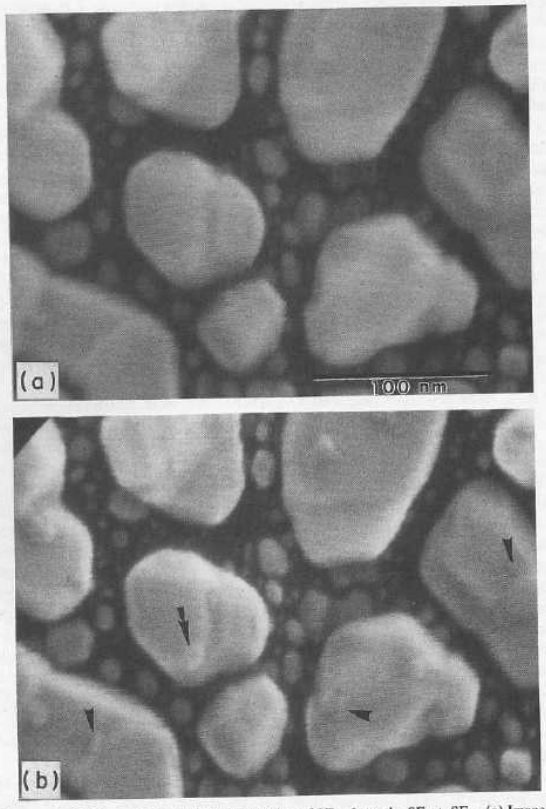

Figure 4.46. Improved contrast by separation of SE_{III} from the $SE_I + SE_{II}$. (a) Image of gold islands on graphite with $SE_I + SE_{II} + SE_{III}$ obtained with conventional E–T operation. (b) $SE_I + SE_{II}$ only, with SE_{III} suppressed by the use of a low secondary-yield shield. Note improved contrast of small features indicated by arrows (Peters, 1984; micrographs courtesy of K.-R. Peters).

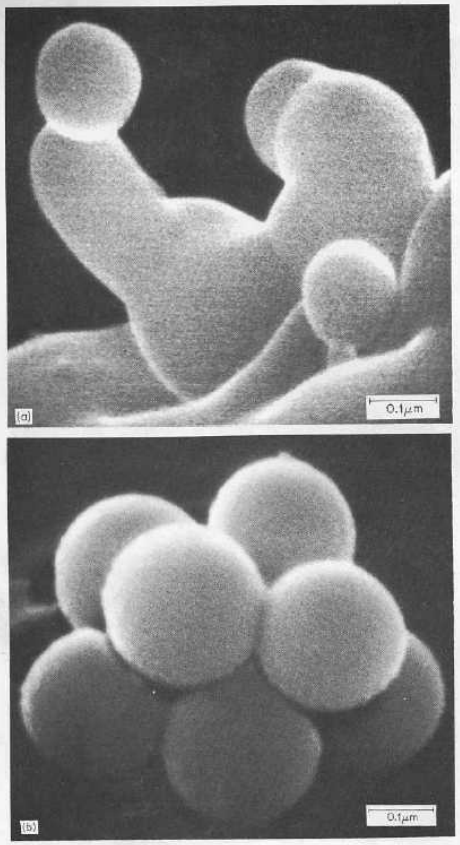

FIG. 6.7 High-resolution secondary electron images. At these magnifications, the entire field of view is involved in the interaction. (*a*) LaB_6 following electron emission (not metallized) (*Broers 1970. Courtesy of IITRI.*); (*b*) 0.26-μm latex balls, coated with Au-Pd alloy, on ~2000-Å self-supporting Al film on a TEM specimen grid. (*Broers 1969b. Courtesy of Rev. Sci. Instrum.*)

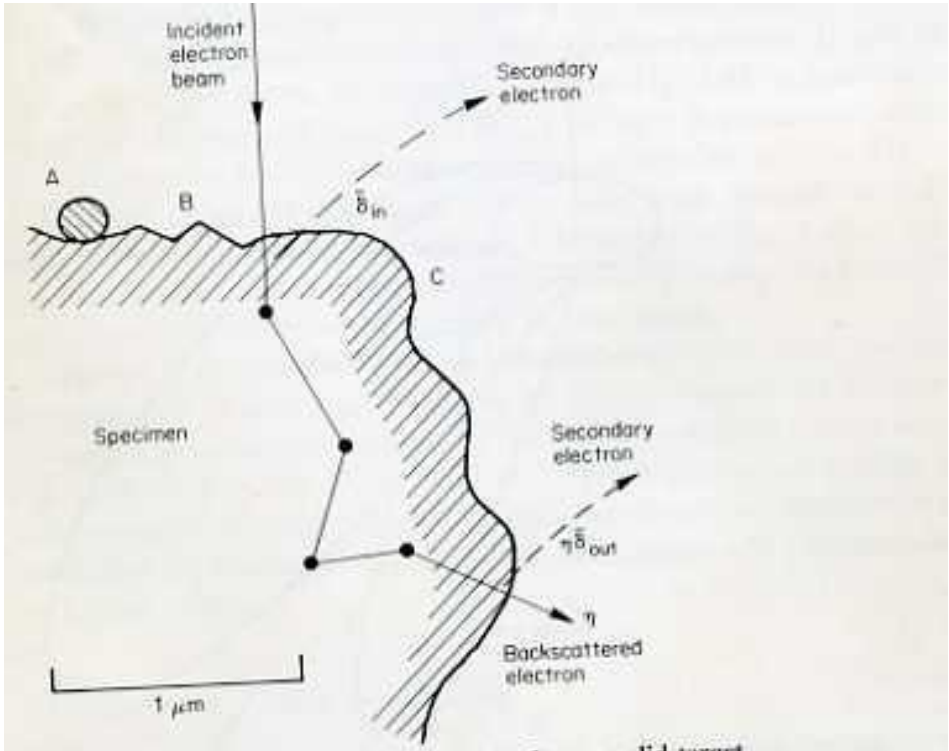

FIG. 3.17 Secondary electron emission from a solid target.

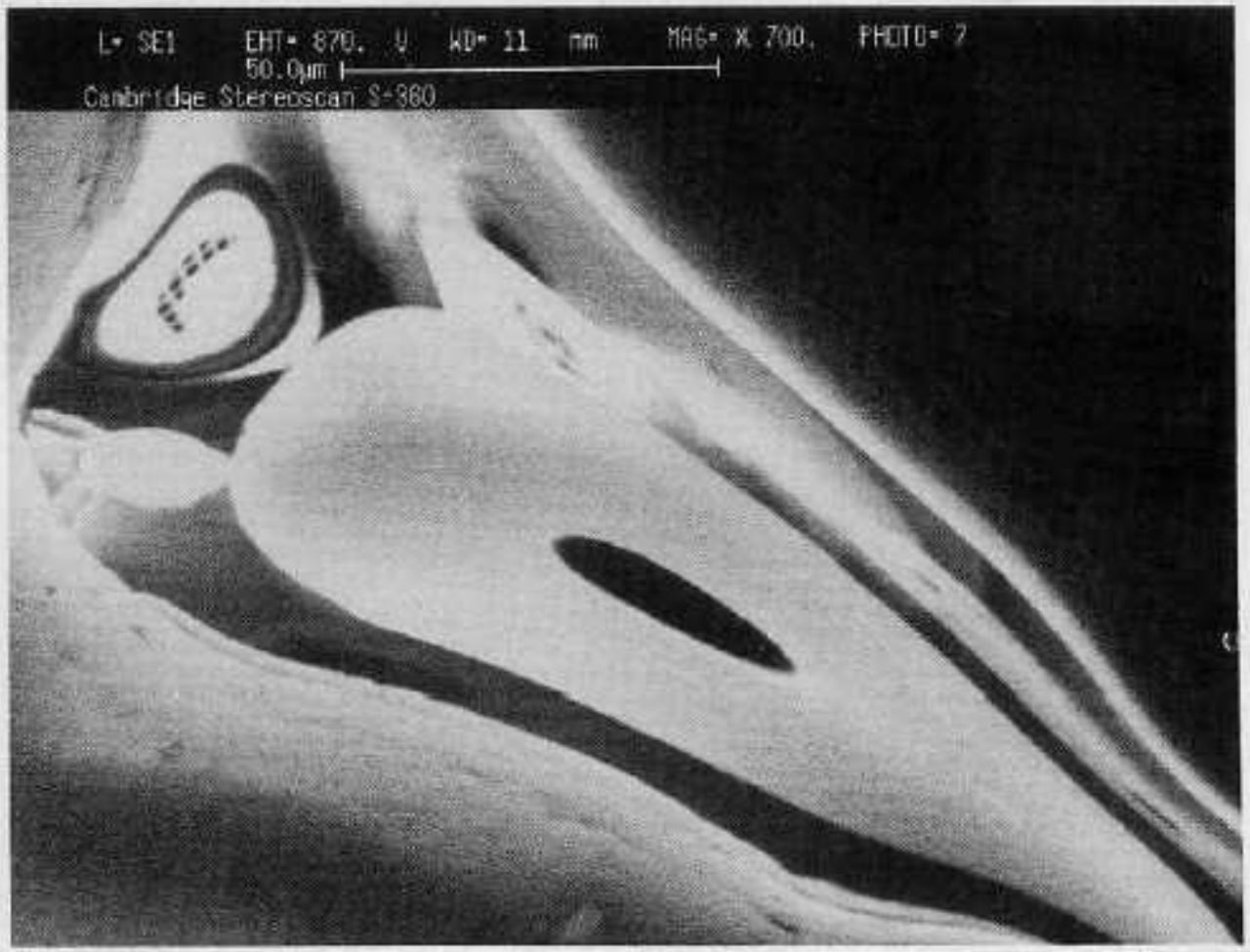

Figure 4.62. Extreme specimen charging, in which the beam is reflected off the specimen and scans the specimen chamber, producing a highly distorted "fisheye lens" view of the polepiece, the Faraday cage of the E–T detector, and the chamber walls.

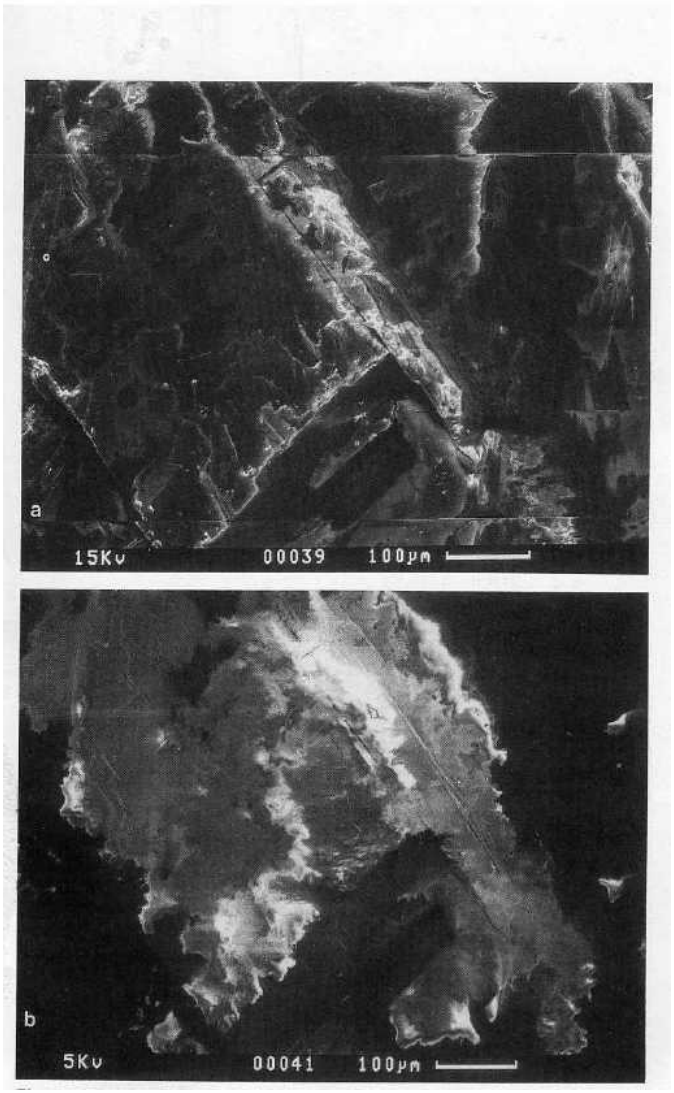

Figure 4.63. Charging observed during SEM imaging of an uncoated calcite crystal. (a) $E_0 = 15$ keV; note the bright/dark regions and the scan discontinuities. (b) $E_0 = 5$ keV; the scanned image is now stable, but the bright/dark voltage contrast dominates the true features of the image. (c) $E_0 = 1.5$ keV; operation at the E_2 crossover point produces a stable image in which topographic contrast showing the true features of the specimen is evident. The bright area on the tilted top surface shows that not all regions of charging can be simultaneously controlled.

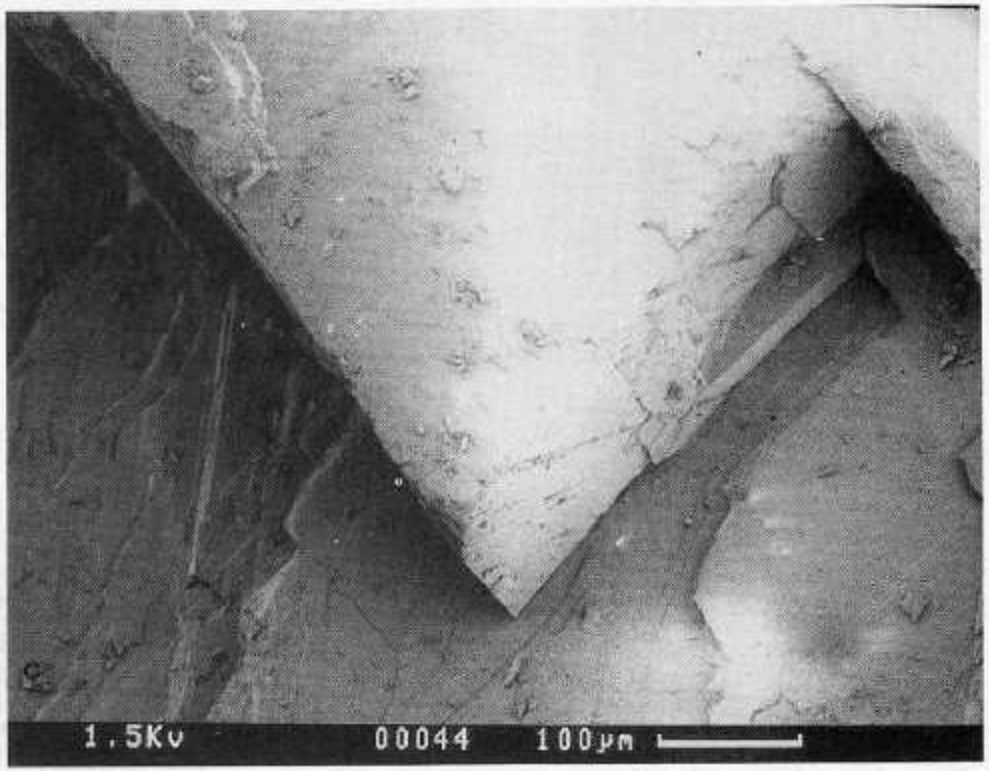

Figure 4.63. (Continued).

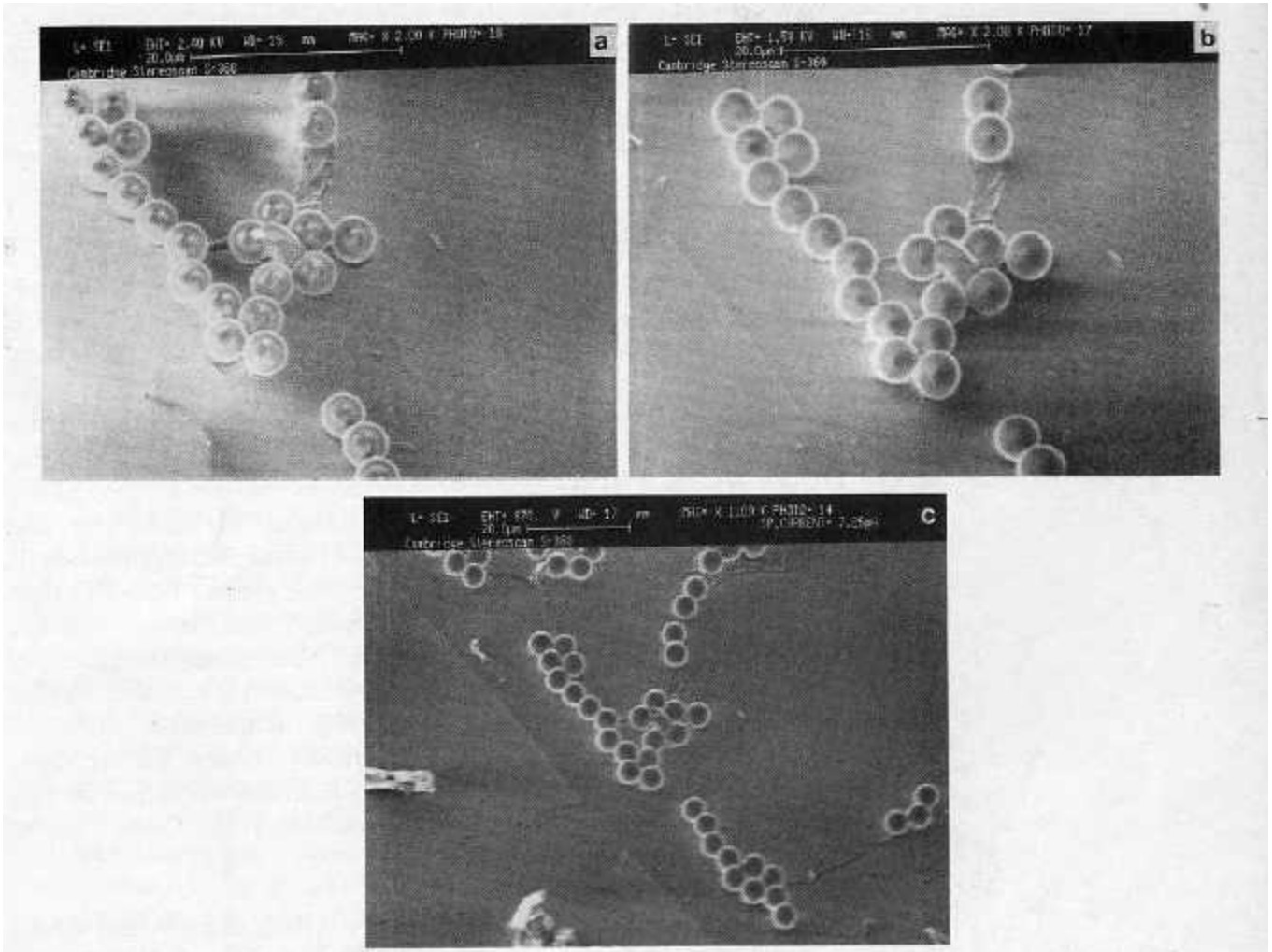

Figure 4.64. Charging that could be mistaken as a specimen feature. (a) The polymer spheres seem to show a complicated interior structure; $E_0 = 2.4$ keV. (b) At $E_0 = 1.53$ keV, the structure has changed into an "pupil", making each sphere look like an "eye". (c) At $E_0 = 0.87$ keV and a reduction in magnification of a factor of two to reduce the dose per unit area, the charging artifact has been eliminated.

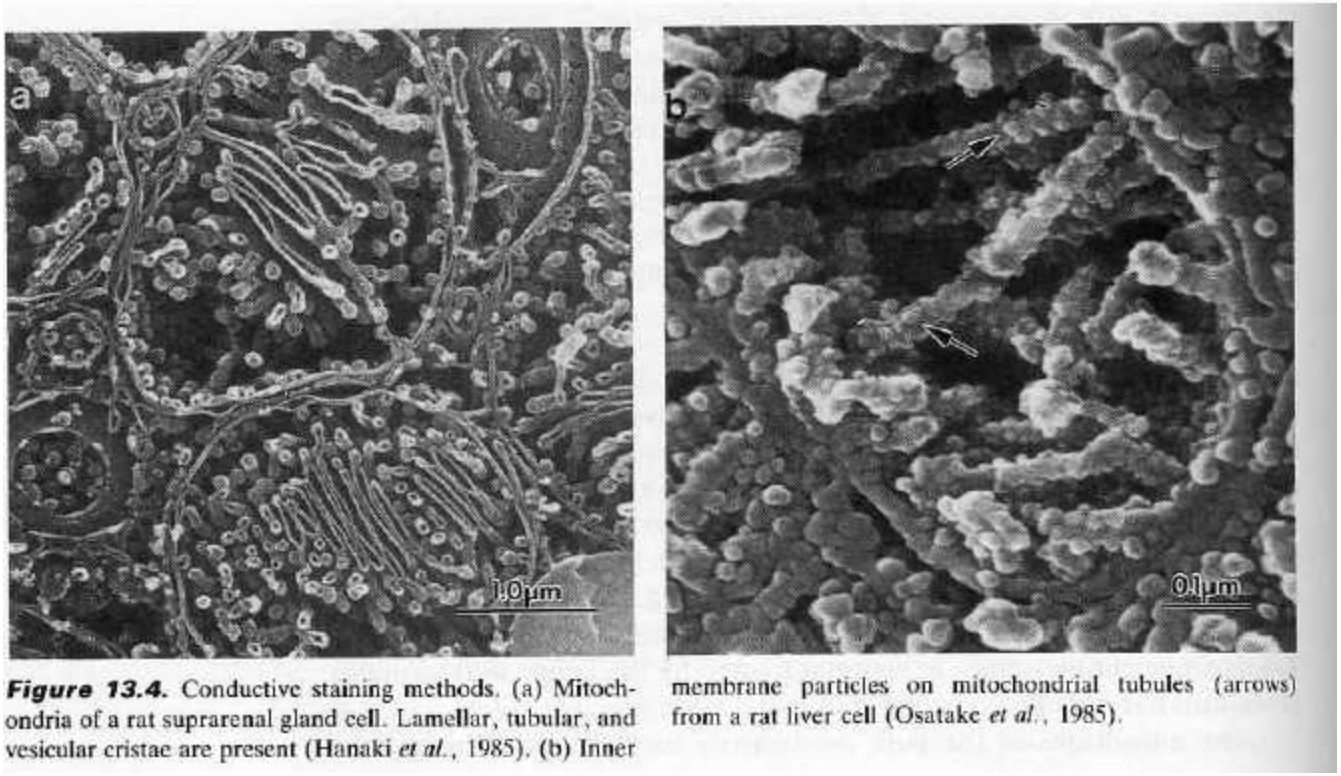

Figure 13.4. Conductive staining methods. (a) Mitochondria of a rat suprarenal gland cell. Lamellar, tubular, and vesicular cristae are present (Hanaki *et al.*, 1985). (b) Inner membrane particles on mitochondrial tubules (arrows) from a rat liver cell (Osatake *et al.*, 1985).

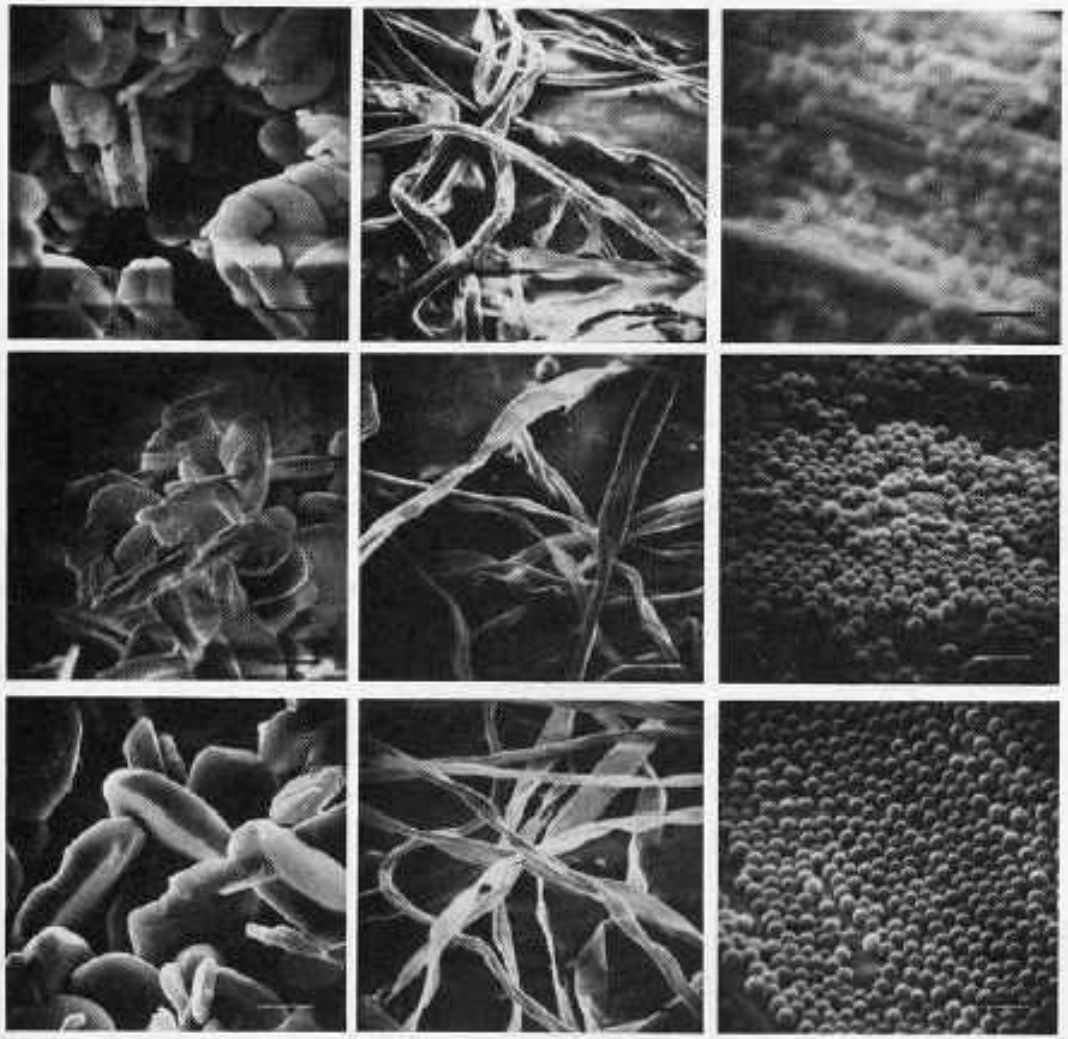

Figure 13.25. Comparison of uncoated, evaporative-coated, and sputter-coated nonconductors. Left, Al_2O_3; center, cotton wool; right, polystyrene latex spheres. Top row, uncoated; center row, evaporative-coated with 10 nm of gold; bottom row, sputter-coated with 10 nm of gold. Magnification bar = 1 μm.

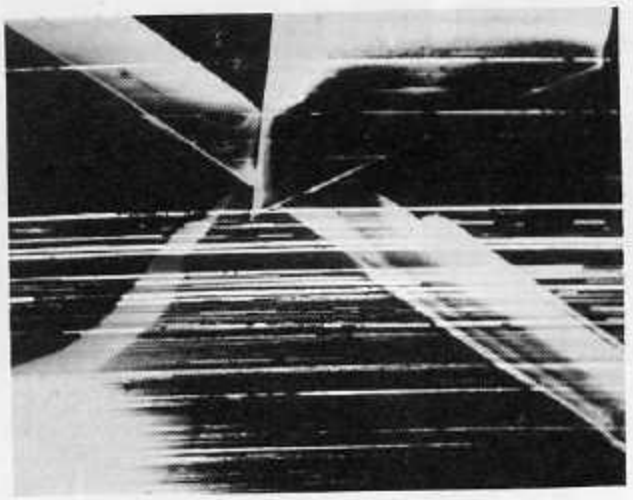

(a)

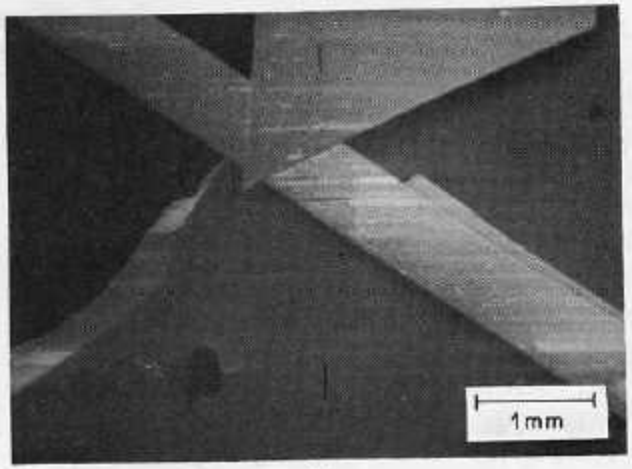

(b)

FIG. 6.36 Secondary electron image of mica at 30 kv. (*a*) At room temperature; (*b*) at 50°C. (*D. C. Joy, unpublished; Metallurgy Dept., Oxford Univ.*)

(a)

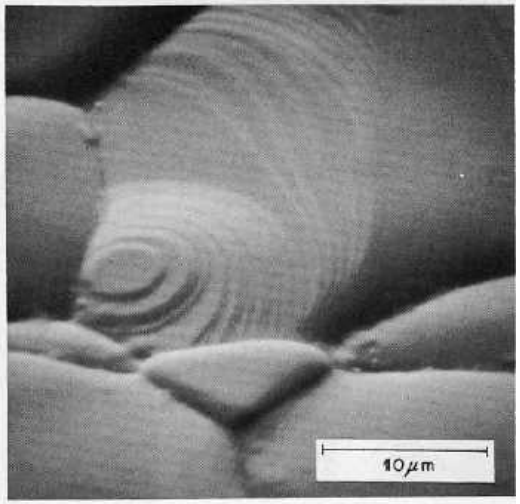

(b)

FIG. 6.37 Uncoated alumina sample viewed at TV scan rate at 16 kv. (*a*) Secondary electron image; (*b*) backscattered electron image. (*Coates and Welter Inc.*)

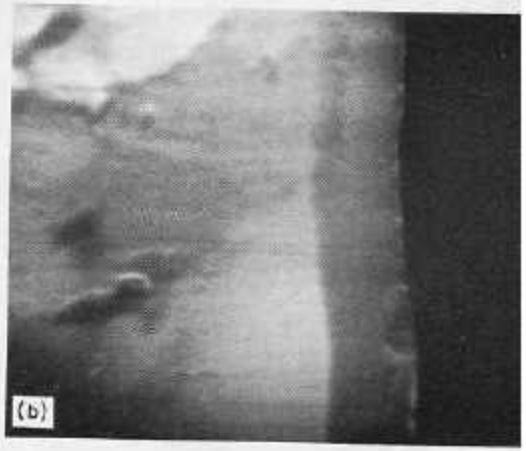

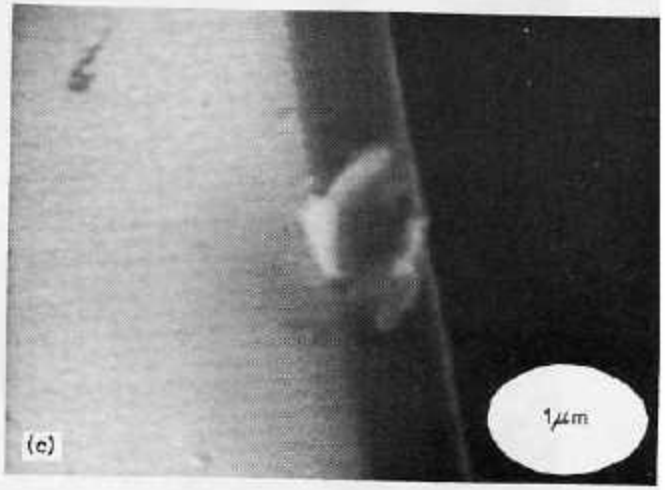

FIG. 6.35 Examination of insulators. Cleaved non-magnetic garnet sample with 0.7-μm surface layer of magnetic garnet. (*a*) Unmetallized, 1.7×10^{-10} amp at 20 kv; 20-sec exposure; note charge effects; (*b*) 3.5×10^{-11} amp by 100-sec exposure; the charge effects are reduced; (*c*) the upper surface is metallized; 6×10^{-11} amp by 40-sec exposure; the charging has been eliminated.

STEREO IMAGING

Measure X, Y coordinates of 2 points relative to some feature in both pictures [rotated by α about Y-axis]

$$Z = P/2M \sin \alpha/2$$

Where

M = Magnification

$Mx = XL - P/2 = XR + P/2$

$My = YL = YR$

$P = XL - XR$

L = Left

R = Right

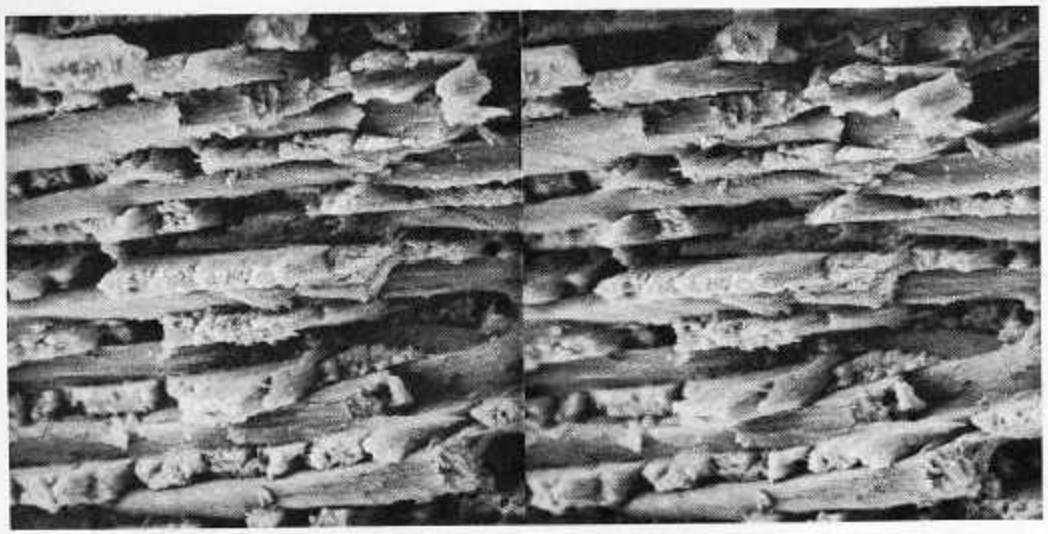

FIG. 11.4 Fractured sheep dental enamel showing prismatic bundles (emerging) and inter-row sheet regions horizontal. Very little concept of the topography of this rough surface can be gained from examination of one image.

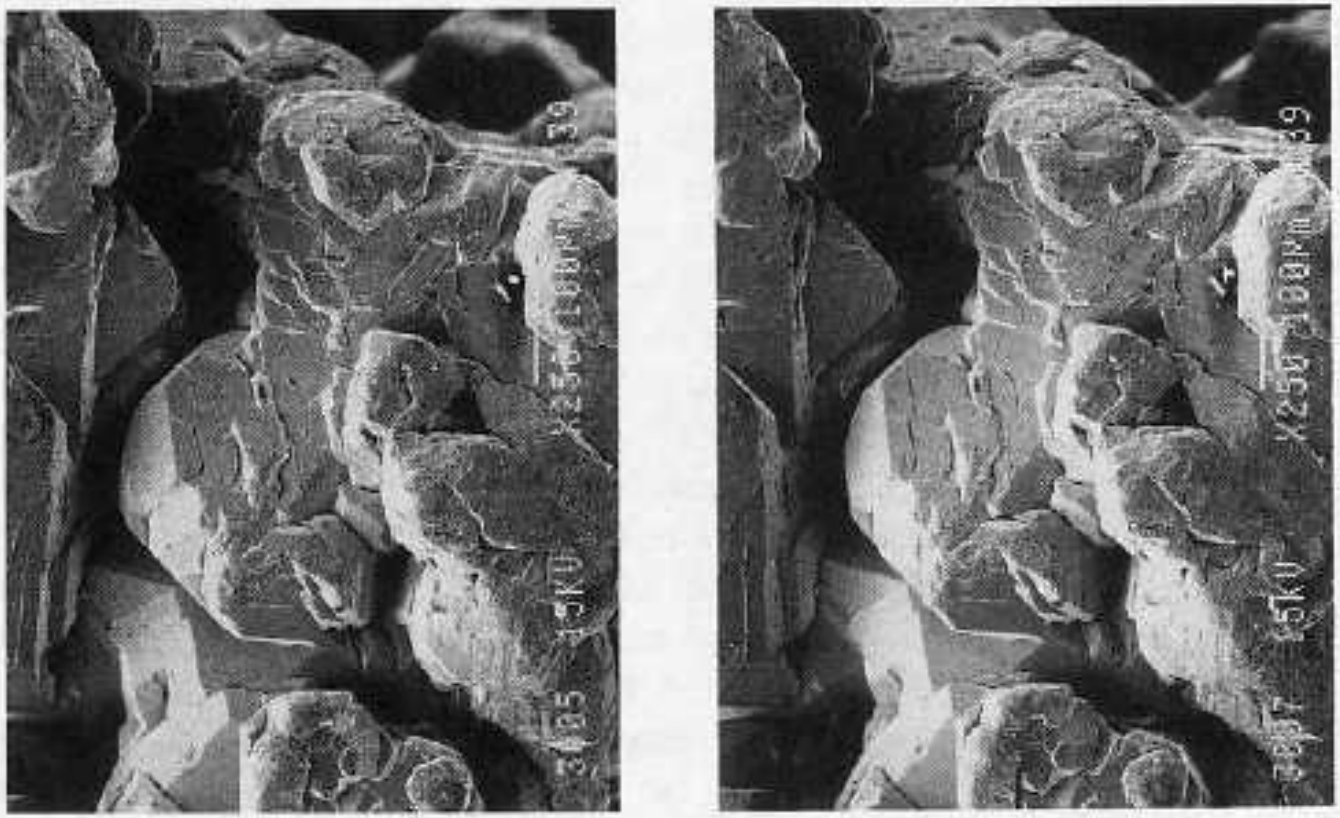

Figure 4.67. Stereo pair of native silver. A typical application of qualitative stereo imaging to view a complicated three-dimensional structure. Illumination is from the left.

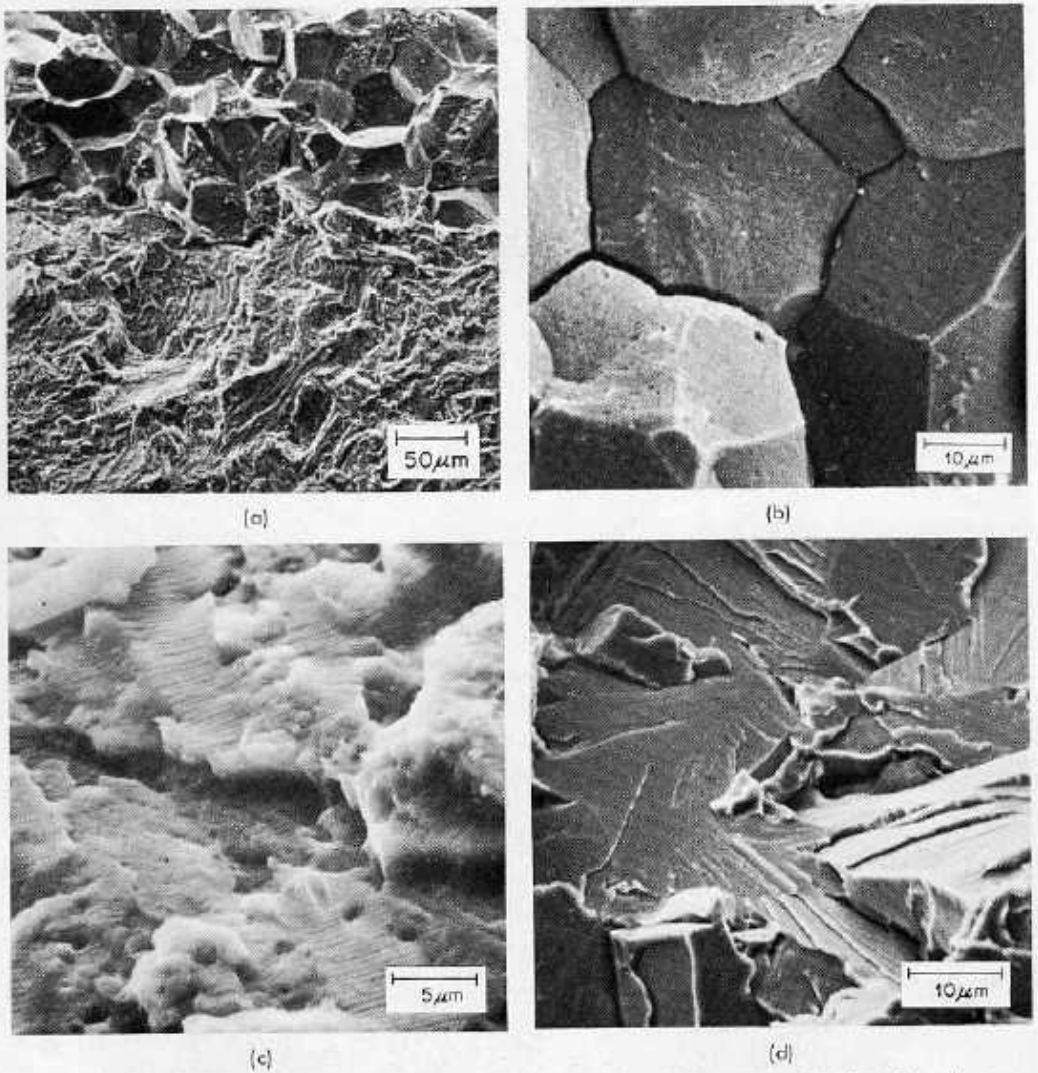

FIG. 9.9 Examples of the SEM applied to the study of fractures. (*a*) Boundary between a fatigue crack and an intergranular fracture in steel; (*b*) detail from (*a*); (*c*) fatigue fracture surface of an Al–Zn–Mg alloy showing striations; (*d*) brittle fracture (at liquid N_2 temperature) of C–Mn semikilled steel. (*Reproduced by permission of the Welding Institute, Abington Hall, Cambridge, Eng.*)

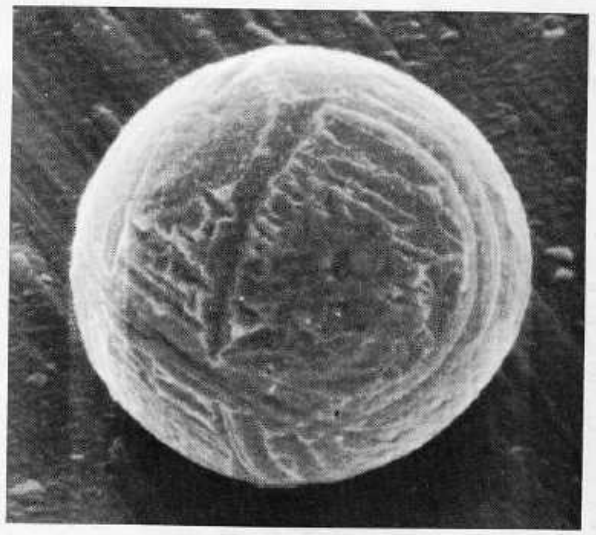

(a)

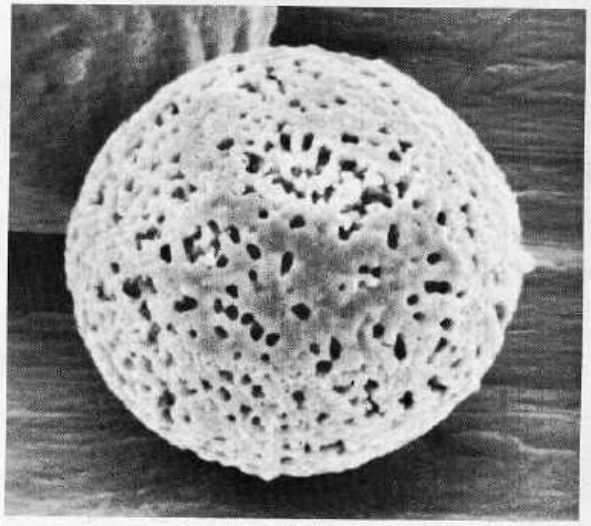

(b)

FIG. 9.10 Iron oxide particles of 20 μm diameter (*a*) unreduced; (*b*) reduced at 700°C. (*Themelis and Gauvin 1962. Courtesy of Am. Inst. Chem. Eng. J.*)

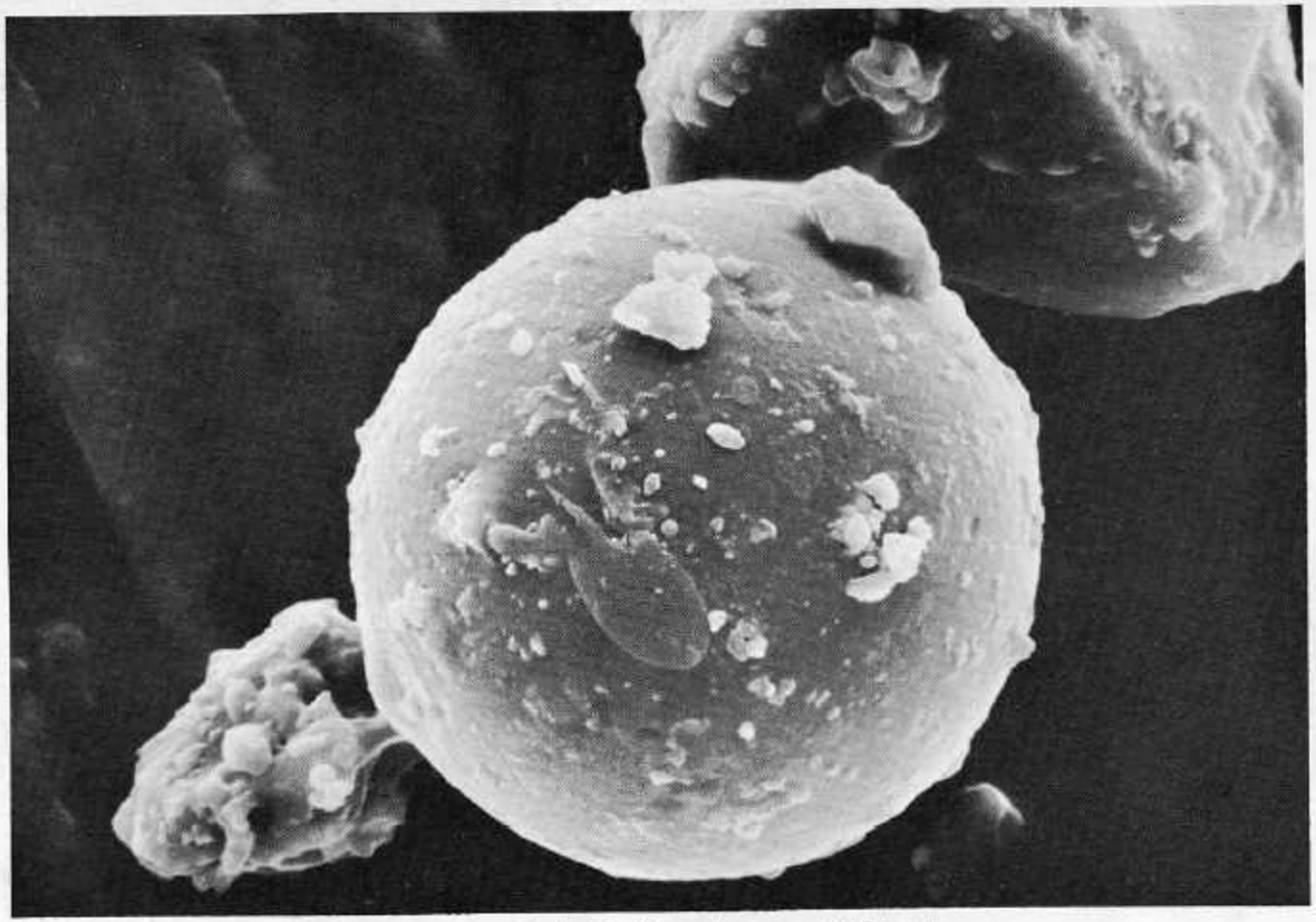

FIG. 9.11 Glass particle of diameter 19 μm from Apollo 11. (Moon dust was sprinkled onto collodion-covered stub and then coated with 300-Å Au using rotating shadowing unit.) (*R. B. Bolon, General Electric Co. Corporate Research and Development.*)

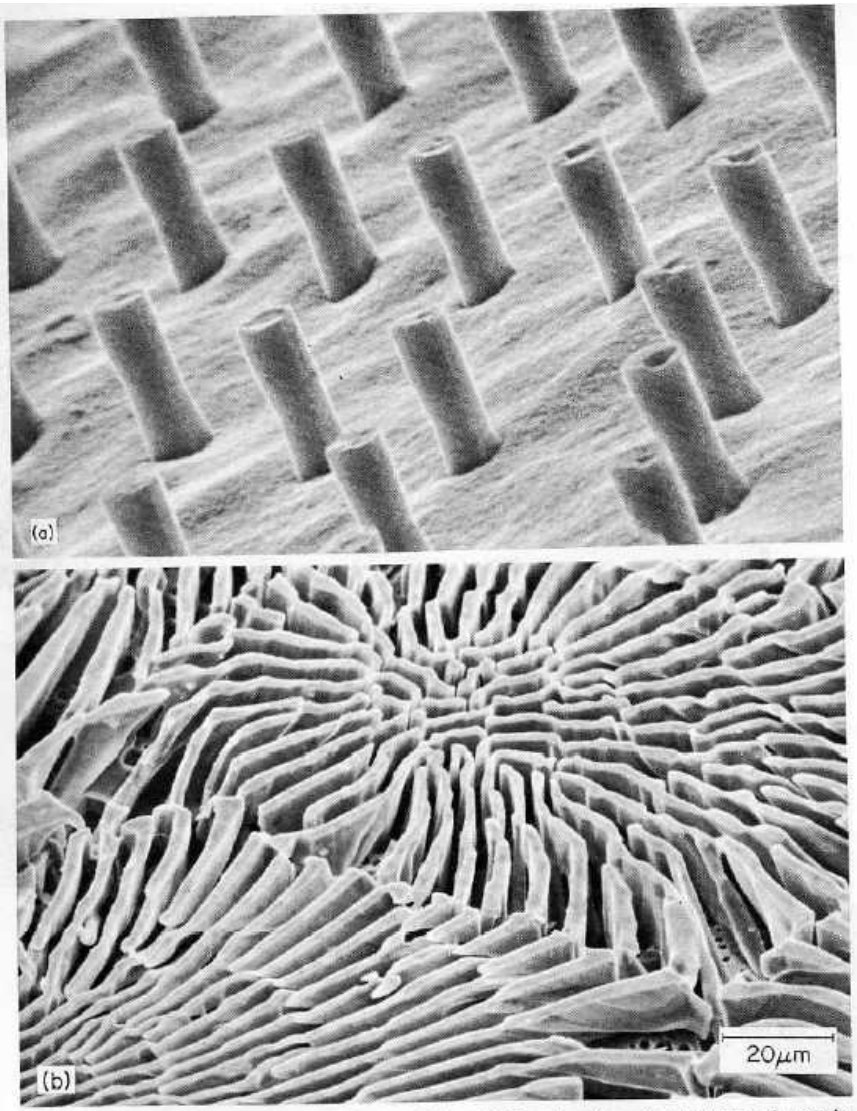

FIG. 9.13 Deeply etched eutectic materials. (*a*) Tungsten fibers in uranium oxide matrix, formed by unidirectional solidification of the melt (diameter of fibers = 1 μm; $\theta = 10°$). (*Gerdes, Chapman, and Clark 1970. Courtesy of Science.*) (*b*) Cells of chromium (molybdenum) plates in NiAl-Cr (6.0 Mo) eutectic solidified at 0.5 iph; $\theta = 30°$. (*Cline et al. 1971. Courtesy of Met. Trans.*)

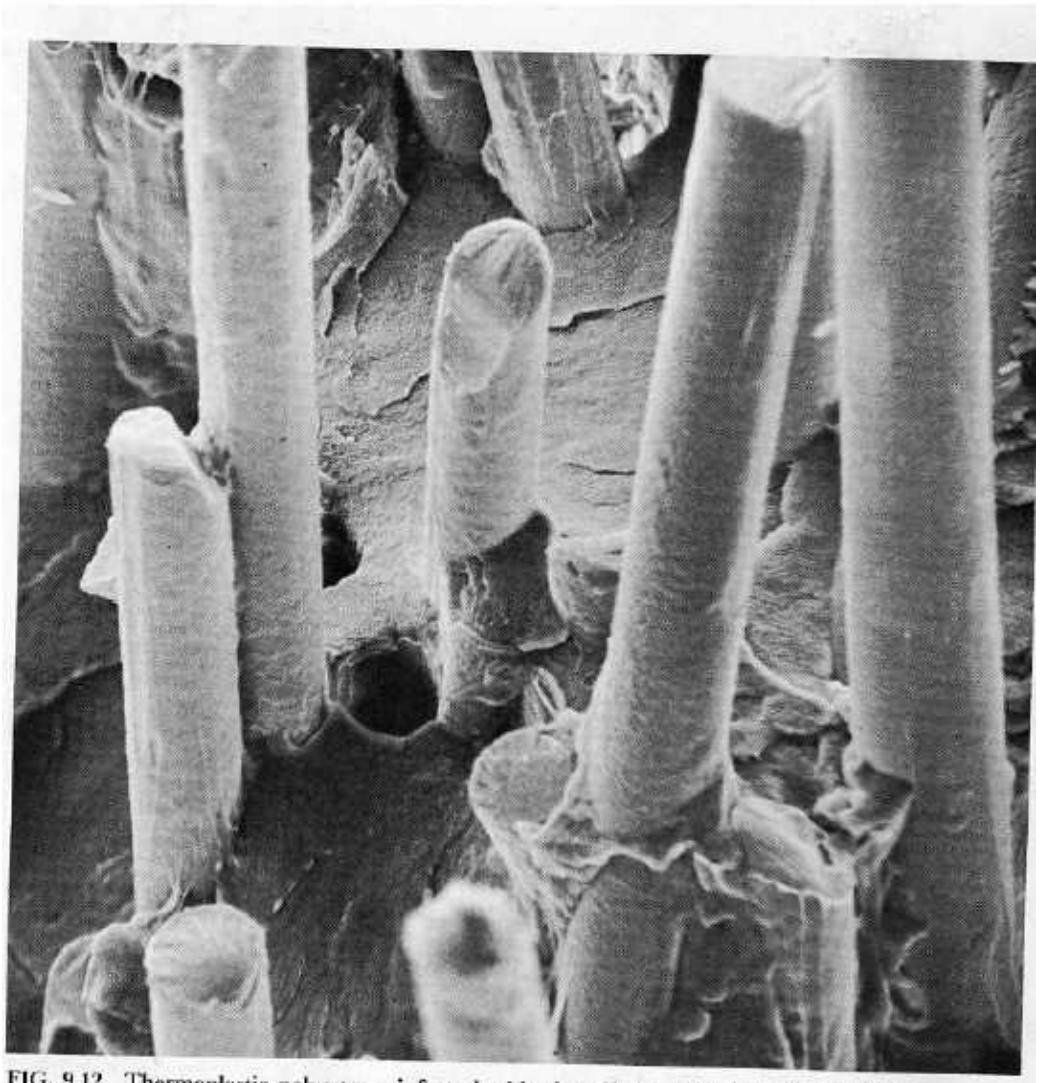

FIG. 9.12 Thermoplastic polyester reinforced with glass fibers. Diameter of glass fiber = 5 μm. (*E. H. Christopherson, General Electric Co. Corporate Research and Development.*)

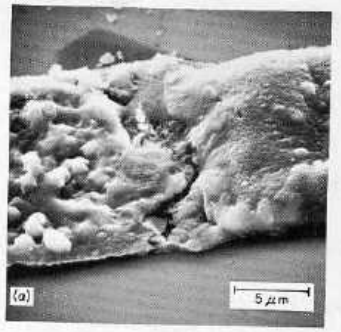

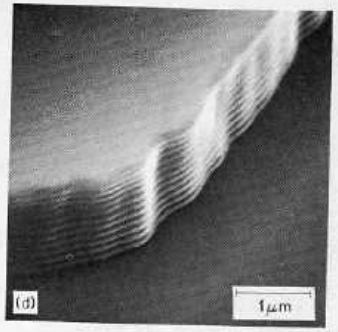

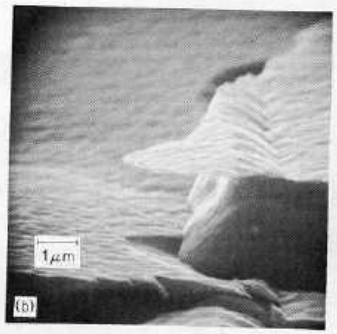

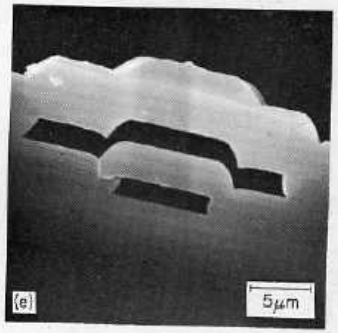

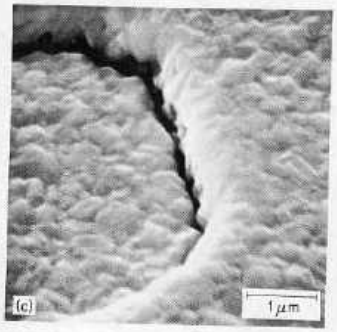

FIG. 9.14 Examples taken from device fabrication and testing. (*a*) Al conductor damaged by electromigration; $\theta = 45°$. (*b*) Passivating glass layer of thickness 0.3 μm over an Al film of thickness 1 μm damaged during heat-cycling of the device (metallized with Au). $\theta = 45°$. (*c*) Discontinuity of Al film where it passes over a step in an underlying SiO_2 surface. ((*b*) and (*c*): *E. K. Brandis unpublished; IBM, Hopewell Junction, N.Y.*) (*d*) Edge of exposed and developed positive photoresist showing ridges caused by standing waves in the monochromatic illumination (metallized with Au). (*Fried, Flachbart et al. 1970. Courtesy of J. Electrochem. Soc.*) (*e*) Multi layer integrated circuit which was cleaved to show the internal structure. The voids are where the aluminum conductors were etched away, to leave the quartz insulating layers; $\theta = 90°$. (*P. Beaufrere; IBM Essonnes Plant, France.*)

FIG. 9.14 Examples taken from device fabrication and testing. (*a*) Al conductor damaged by electromigration; $\theta = 45°$. (*b*) Passivating glass layer of thickness 0.3 μm over an Al film of thickness 1 μm damaged during heat-cycling of the device (metallized with Au). $\theta = 45°$. (*c*) Discontinuity of Al film where it passes over a step in an underlying SiO_2 surface. ((*b*) and (*c*): *E. K. Brandis unpublished; IBM, Hopewell Junction, N.Y.*) (*d*) Edge of exposed and developed positive photoresist showing ridges caused by standing waves in the monochromatic illumination (metallized with Au). (*Fried, Flachbart et al. 1970. Courtesy of J. Electrochem. Soc.*) (*e*) Multi layer integrated circuit which was cleaved to show the internal structure. The voids are where the aluminum conductors were etched away, to leave the quartz insulating layers; $\theta = 90°$. (*P. Beaufrere; IBM Essonnes Plant, France.*)

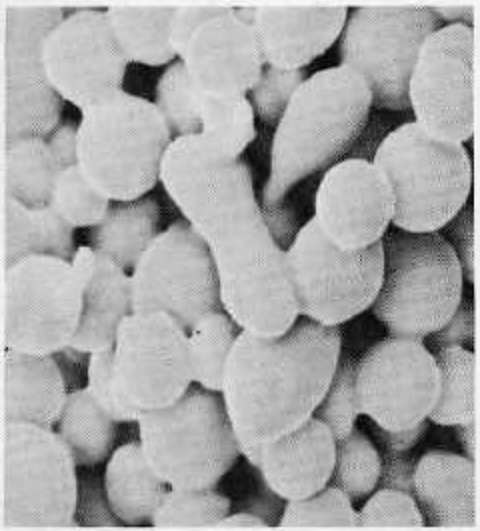

(a)

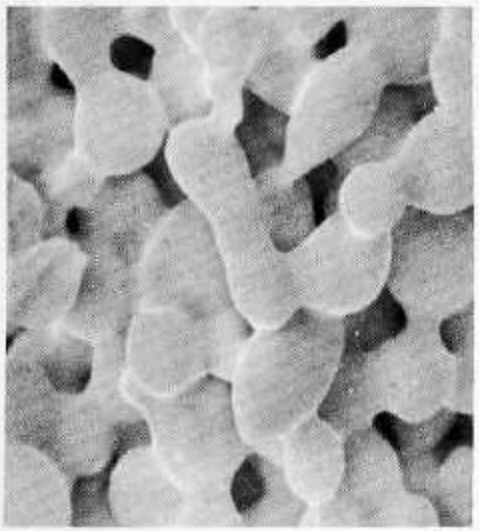

(b)

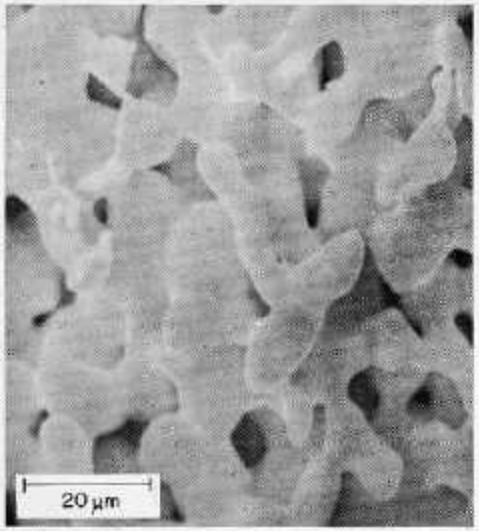

(c)

FIG. 9.17 Thermal etching of nickel particles (*a*) at 1000°C; (*b*) at 1300°C and held 8 min; (*c*) as (*b*), but held 20 min. (*Fulrath 1972. Courtesy of IITRI.*)

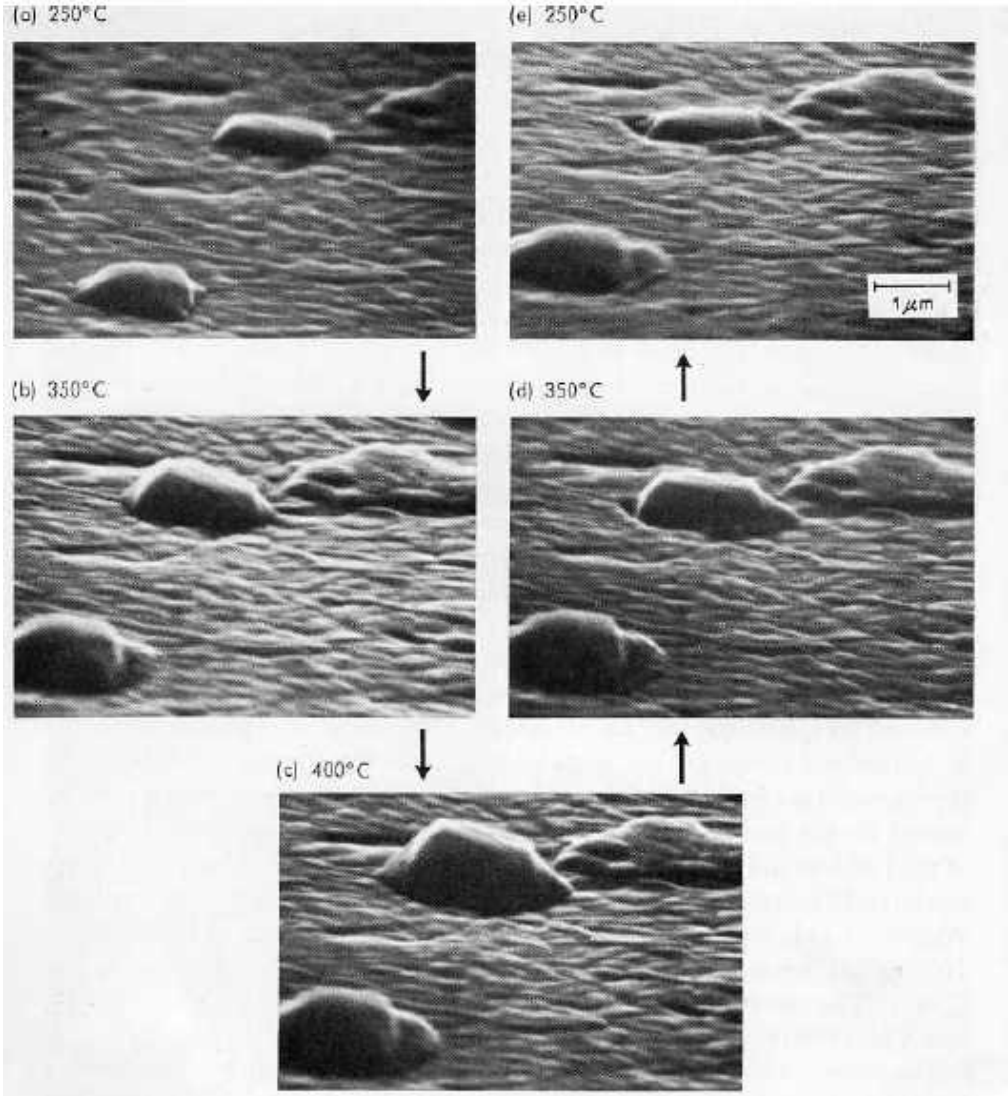

FIG. 9.18 Hillock rises and falls during temperature cycling of 0.13-μm Al film on oxidized Si substrate. (*a*) 250°C; (*b*) 350°C; (*c*) 400°C; (*d*) 350°C; (*e*) 250°C. Note the appearance of a groove around the hillock in the final micrograph. (*Lahiri and Wells 1969. Courtesy of Appl. Phys. Lett.*)

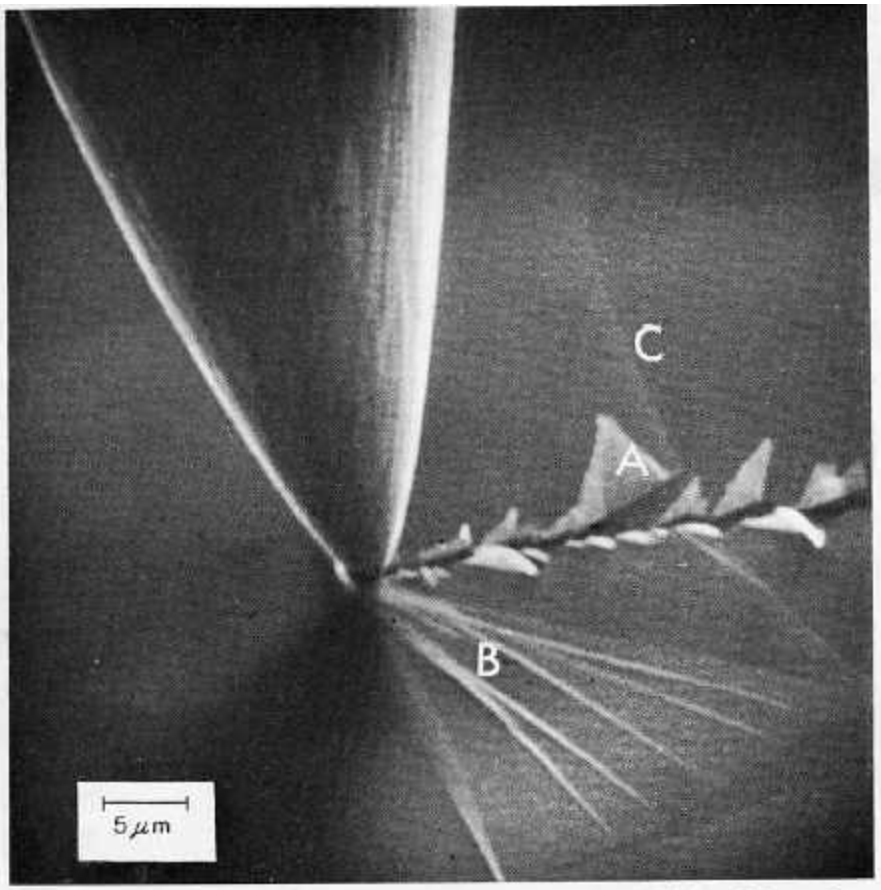

FIG. 9.20 Stylus sliding on the basal plane of graphite. (*A*) Flaking of the surface; (*B*) peeling; (*C*) a cleavage step. (*Skinner, Gane, and Tabor 1971. Courtesy of Nat. Phys. Sci.*)

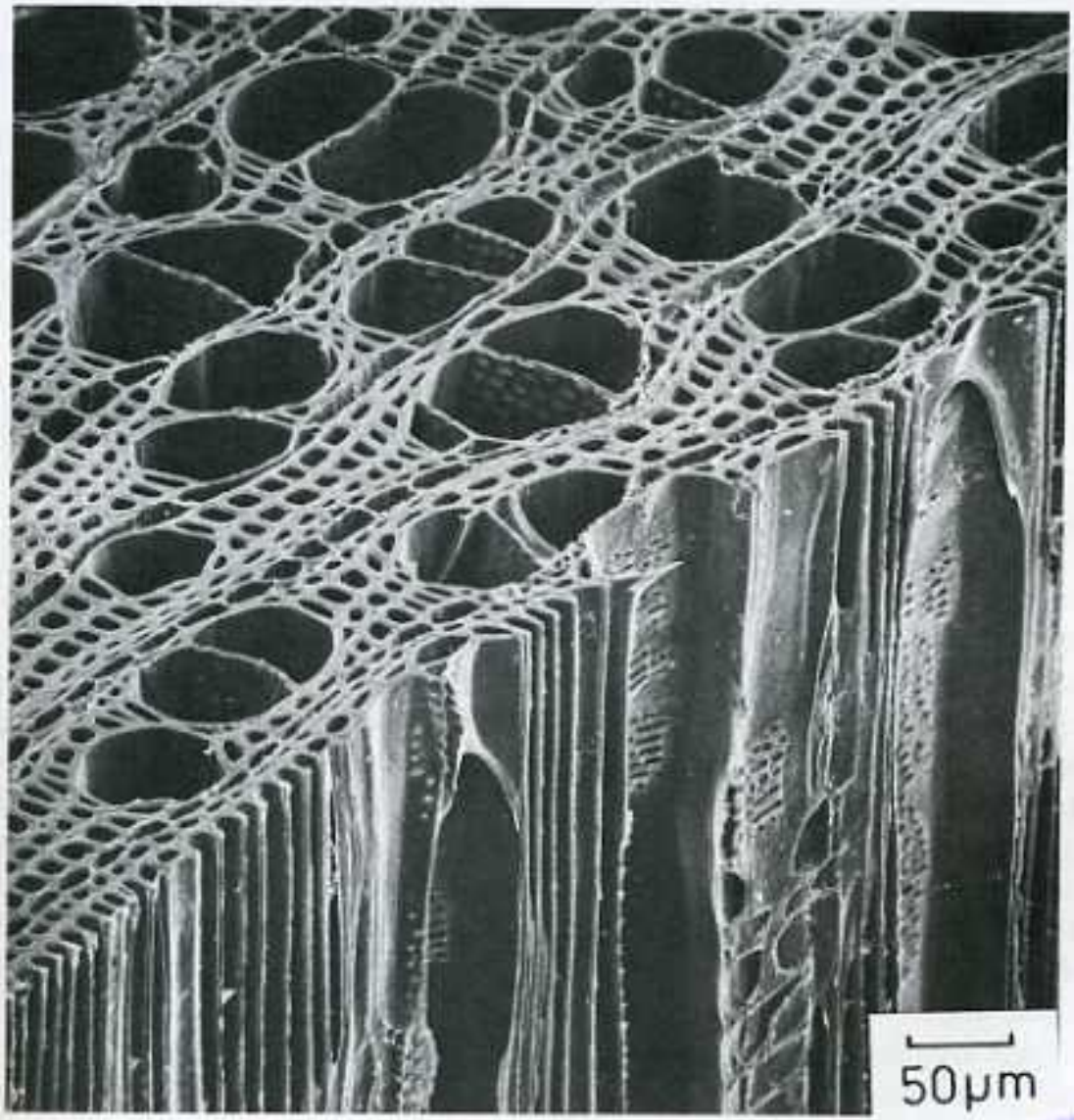

Figure 12.12. Transverse and radial longitudinal surfaces of the wood of *Notofagus fusca* (Exley *et al.*, 1974).

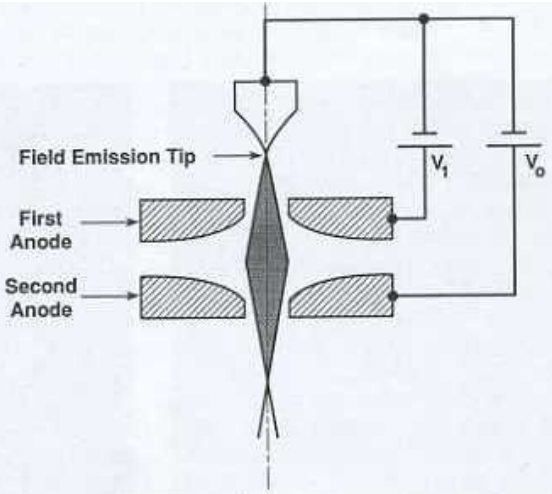

Figure 2.12. Schematic diagram of the Butler triode field emission source. V_1 is the extraction voltage, typically a few kV, and V_0 is the accelerating voltage (adapted from Crewe, 1969).

Brightness and Probe Current. The cathode current density J_c for a cold field emission source strongly depends on the applied field strength, similar to the way thermionic emission is dependent upon temperature. Expressions derived to calculate J_c (Fowler and Nordheim, 1928; Good and Muller, 1956) yield values in the range $J_c = 10^4$–

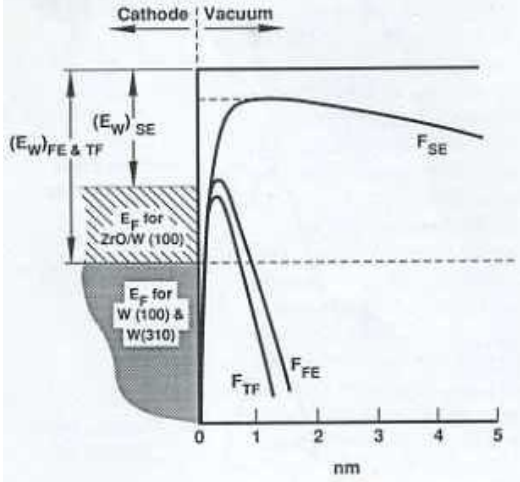

Figure 2.13. Energy-level diagram for cold field emission (FE), thermal field emission (TF), and Schottky emission (SE). Electrons tunnel through the narrow barriers in the FE and TF cases. For the SE case, the sharp tip covers the barrier and the zirconium oxide coating reduces the work function so that electrons can escape over the barrier (adapted from Tuggle *et al.*, 1985).

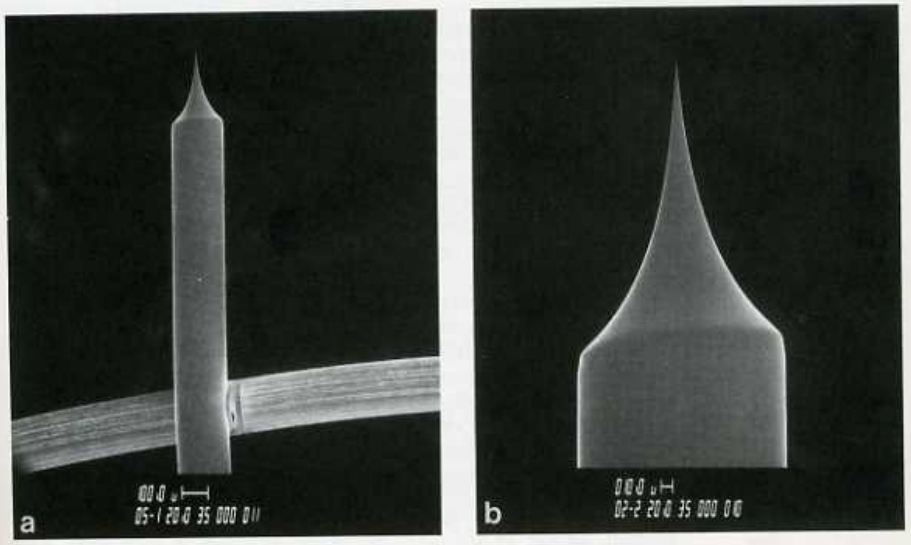

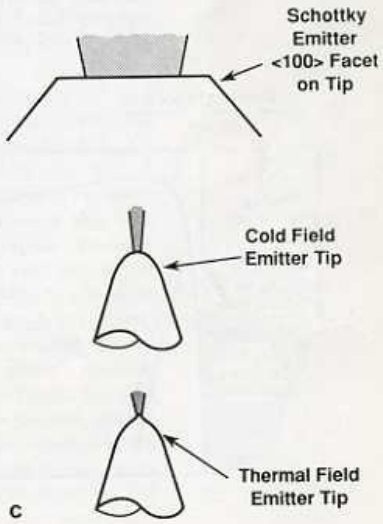

Figure 2.11. Examples of field emission sources. (a) SEM micrograph of ⟨310⟩ single crystal wire spot welded to a tungsten wire. (b) Higher-magnification image of the tip. (c) Schematic diagram comparing tip shapes for the Schottky emitter, cold field emitter, and thermal field emitter (adapted from Tuggle *et al.*, 1985).

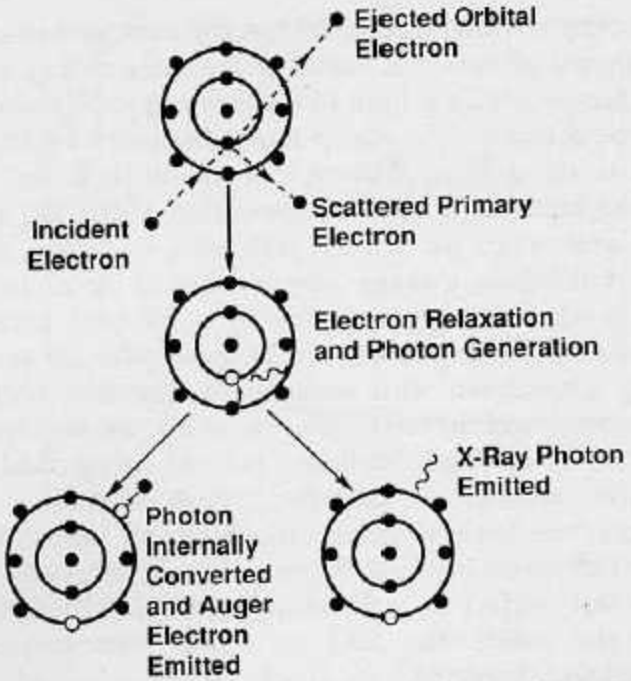

Figure 3.33. Schematic illustration of the process of inner-shell ionization and subsequent de-excitation by electron transitions. The difference in energy between the shells is expressed either by the ejection of an energetic electron with characteristic energy (Auger process) or by the emission of a characteristic x ray.

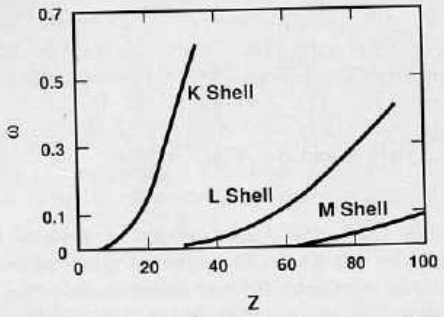

Figure 3.34. Fluorescence yield ω as a function of atomic number for several shells.

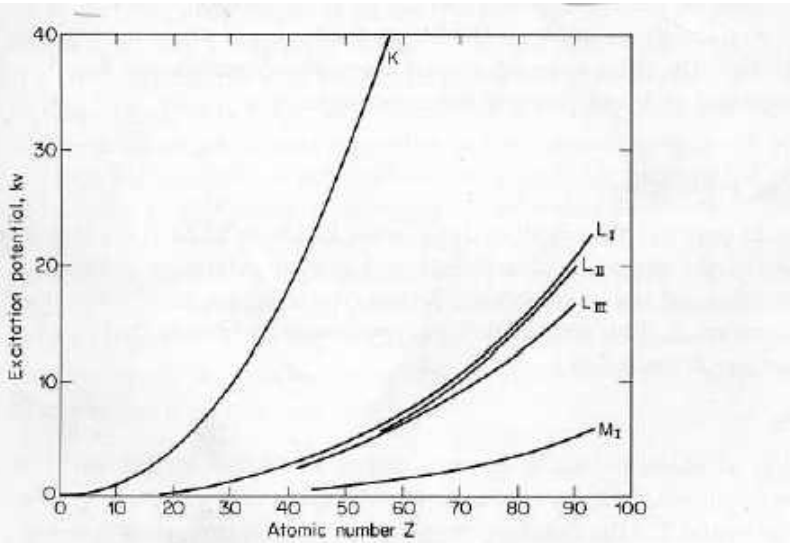

FIG. 10.2 Excitation potential as a function of atomic number.

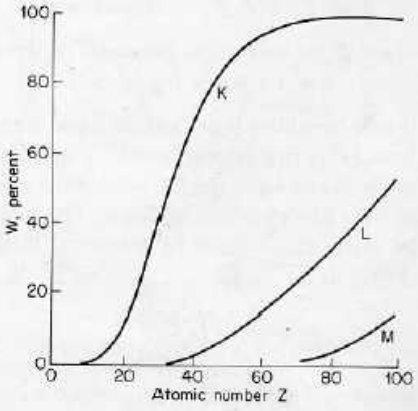

FIG. 10.3 The dependence of fluorescent yield W on atomic number Z.

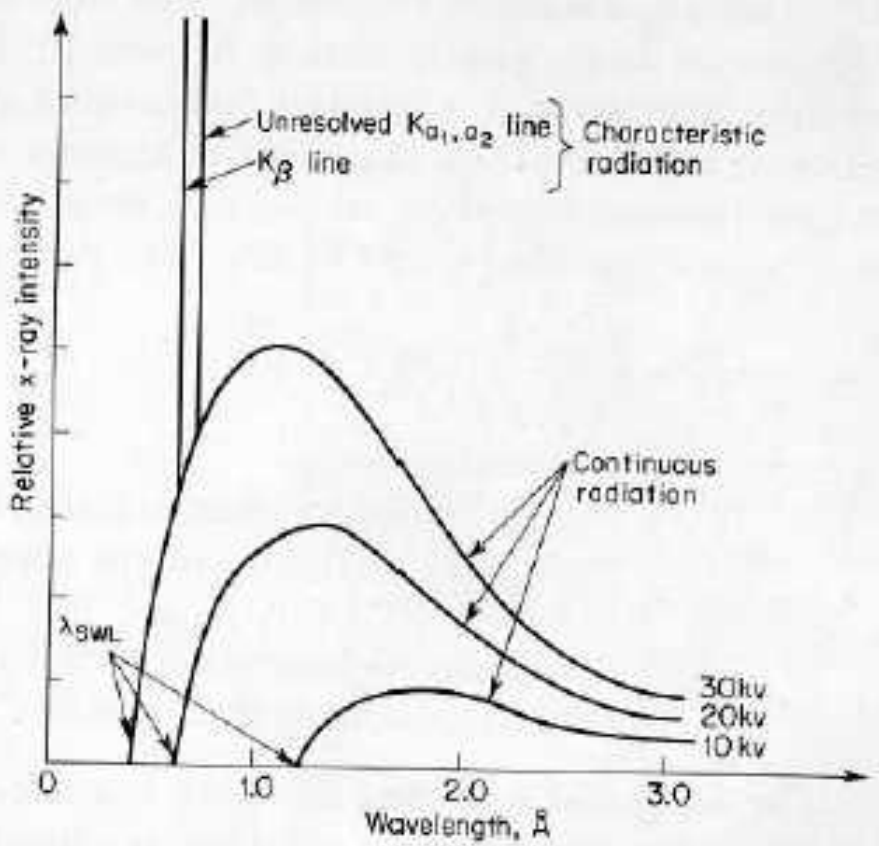

FIG. 10.5 A schematic representation of the continuous and characteristic emission of molybdenum as a function of operating voltage.

$$K = \frac{0.0276A}{Z^{0.889}}, \qquad (3.44)$$

$$\rho R = 0.064(E_0^{1.68} - E_c^{1.68}), \qquad (3.45)$$

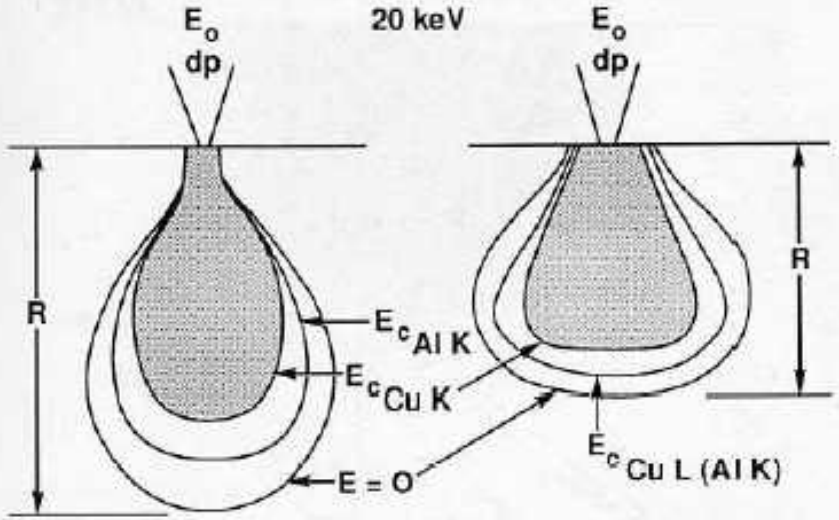

Figure 3.42. Comparison of x-ray production regions from specimens with densities of 3 (left) and 10 g/cm^3 (right).

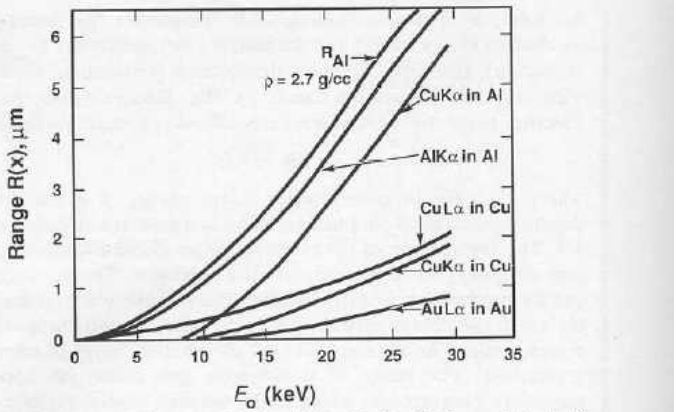

Figure 3.40. X-ray generation range for the Al *Kα*, Cu *Kα*, Cu *Lα*, and Au *Lα* lines generated within aluminum, copper, and gold as a function of incident beam energy.

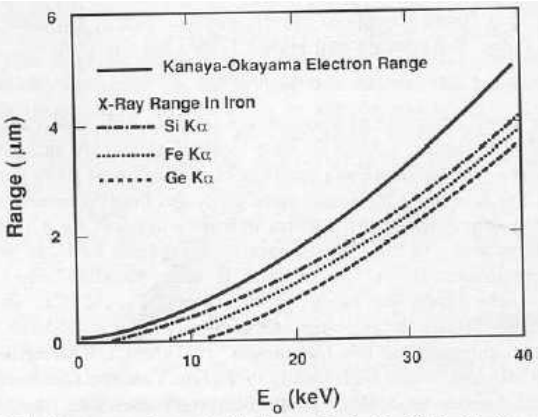

Figure 3.41. X-ray generation range (Andersen–Hasler) for Si *Kα*, Fe *Kα*, and Ge *Kα* in an iron matrix as a function of beam energy.

Table 3.13. X-Ray Energy and Mass Absorption Coefficients for Ni $K\alpha$ in Several Elements

Element (atomic number)	$K\alpha$	$K\beta$	E_{edge}	(μ/ρ) Ni $K\alpha$ (cm^2/g)
Mn (25)	5.895	6.492	6.537	344
Fe (26)	6.400	7.059	7.111	380
Co (27)	6.925	7.649	7.709	53
Ni (28)	7.472	8.265	8.331	59
Cu (29)	8.041	8.907	8.980	65.5

propagating through a slab of thickness t and density ρ, the intensity on the exit surface is attenuated according to the expression

$$\frac{I}{I_0} = \exp -(\mu/\rho)(\rho t), \tag{3.46}$$

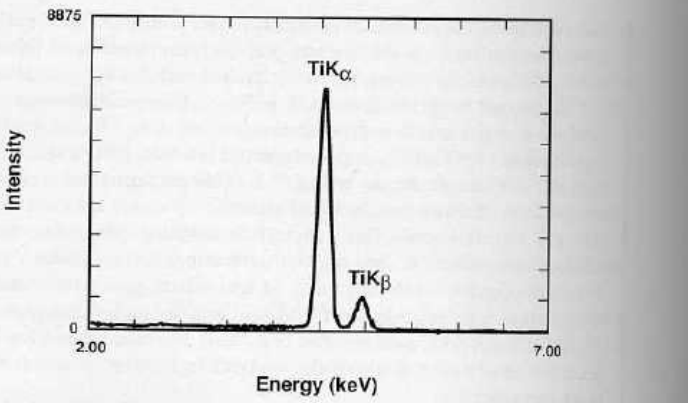

Figure 6.2. Titanium $K\alpha$ and $K\beta$ peaks. $K\alpha = 4.51$ keV. [Ultrathin window (diamond) Si(Li) EDS, 145 eV FWHM at Mn $K\alpha$.]

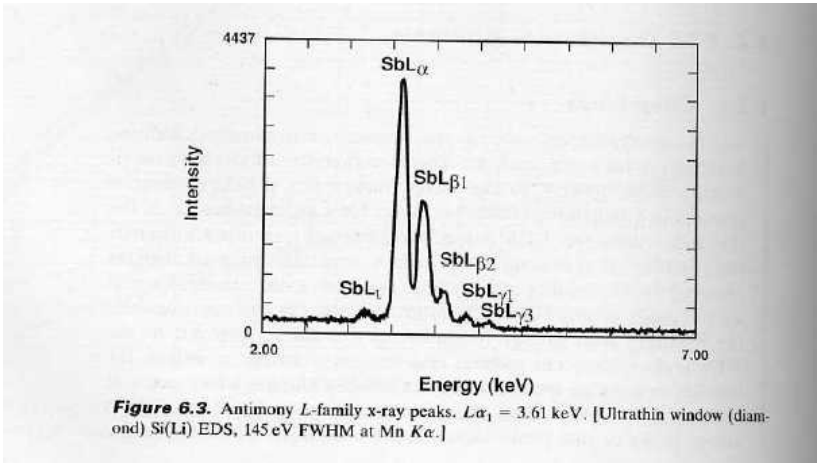

Figure 6.3. Antimony L-family x-ray peaks. $L\alpha_1 = 3.61$ keV. [Ultrathin window (diamond) Si(Li) EDS, 145 eV FWHM at Mn $K\alpha$.]

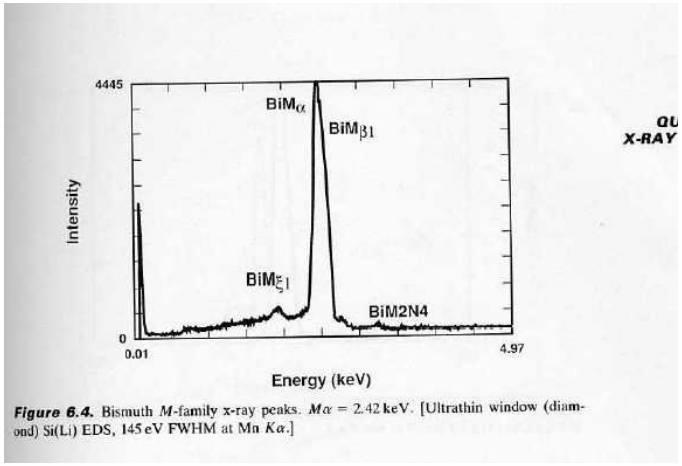

Figure 6.4. Bismuth M-family x-ray peaks. $M\alpha = 2.42$ keV. [Ultrathin window (diamond) Si(Li) EDS, 145 eV FWHM at Mn $K\alpha$.]

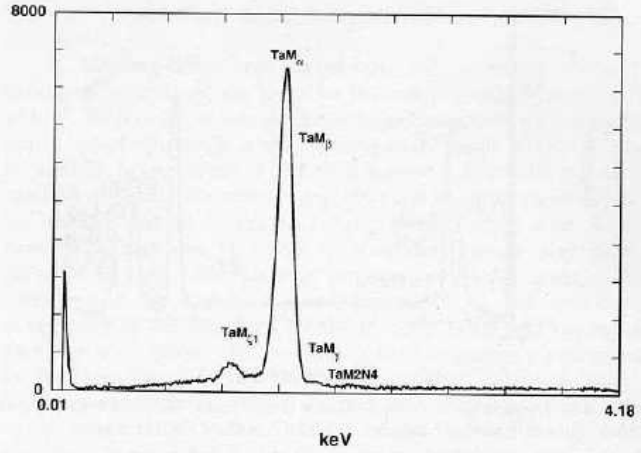

Figure 6.7. Tantalum *M*-family x-ray peaks. $M\alpha = 1.71$ keV. [Ultrathin window (diamond) Si(Li) EDS, 145 eV FWHM at Mn $K\alpha$.]

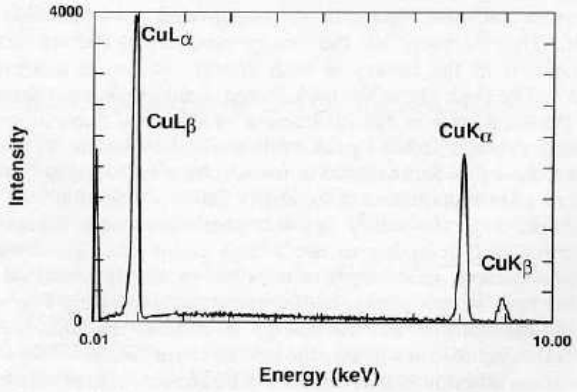

Figure 6.8. Copper *K*- and *L*-family x-ray peaks. $K\alpha = 8.04$ keV; $L\alpha = 0.92$ keV. [Ultrathin window (diamond) Si(Li) EDS, 145 eV FWHM at Mn $K\alpha$.]

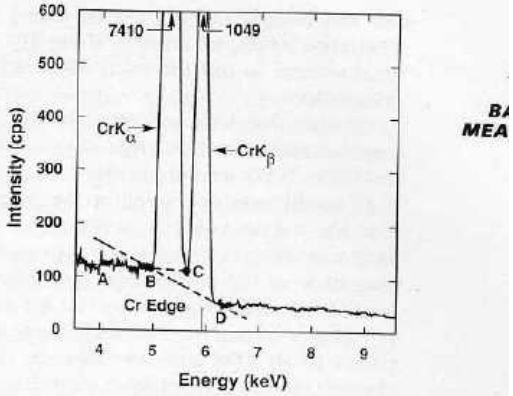

Figure 7.1. EDS background fitting by linear interpolation (points B–C or B–D) or extrapolation (points A–B) in a simple spectrum of chromium (Lifshin, 1975).

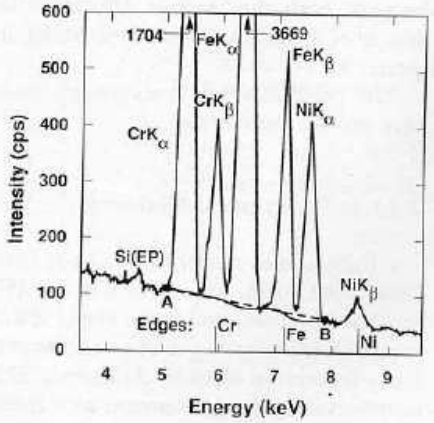

Figure 7.2. EDS background fitting by linear interpolation in a complex spectrum of stainless steel.

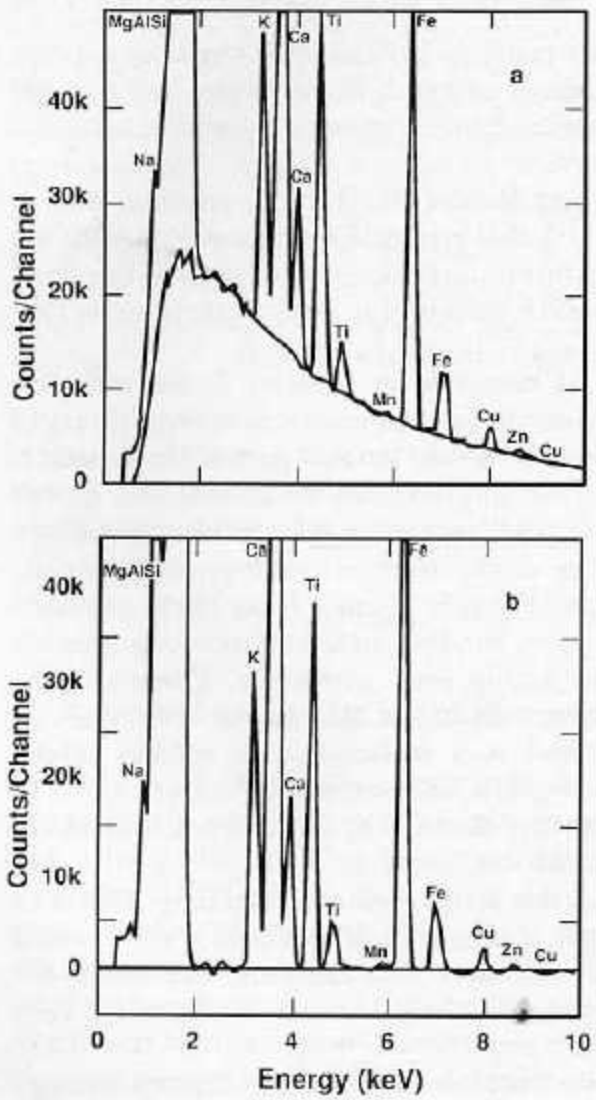

Figure 7.4. Background correction in Kakanui hornblende. (a) Fitted continuum curve calculated by Eq. (7.7); Observed spectrum is superposed. Note the presence of Mn $K\alpha$ peak at 5.9 keV. The concentration of Mn is less than 700 ppm. (b) Background subtracted.

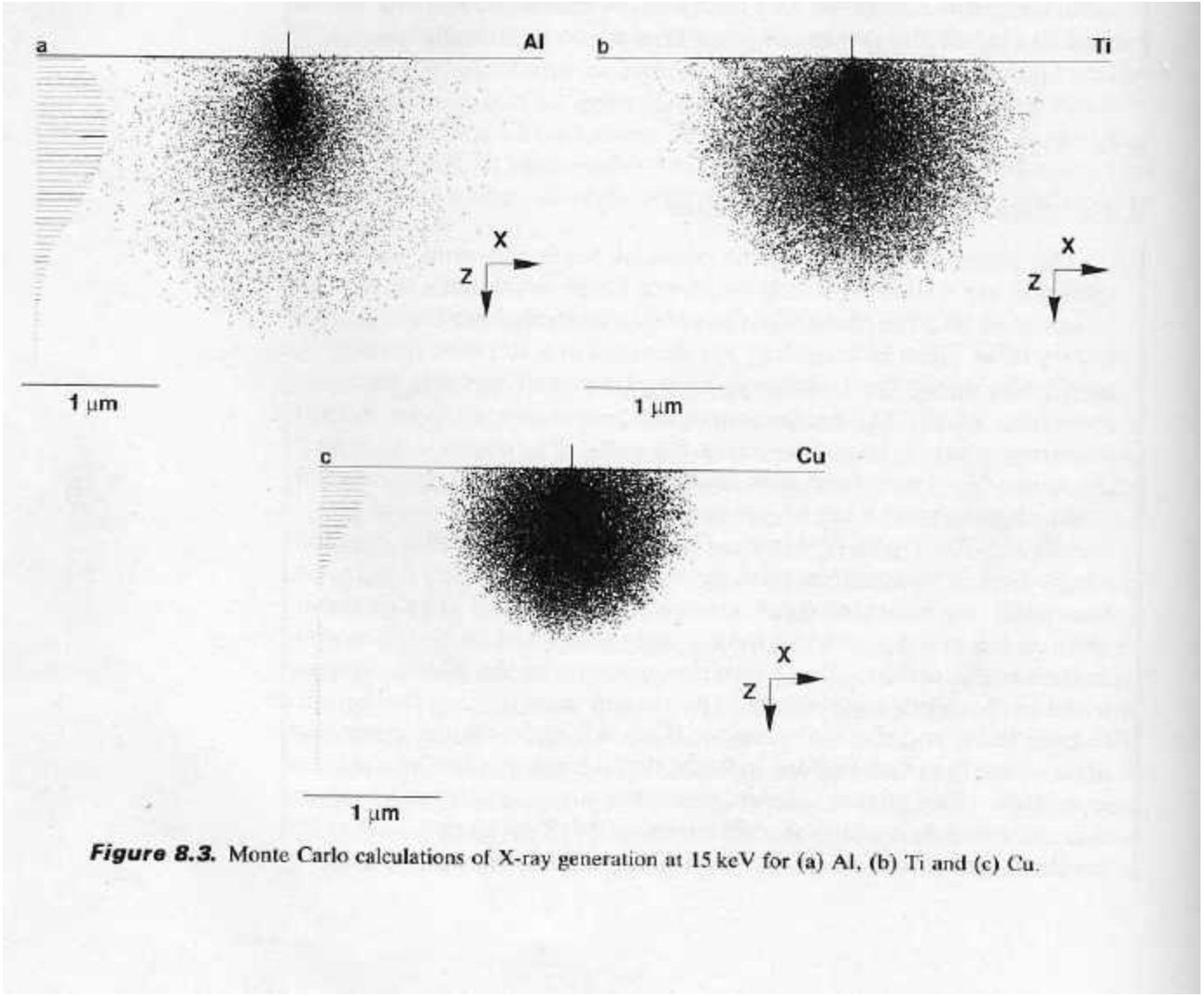

Figure 8.3. Monte Carlo calculations of X-ray generation at 15 keV for (a) Al, (b) Ti and (c) Cu.

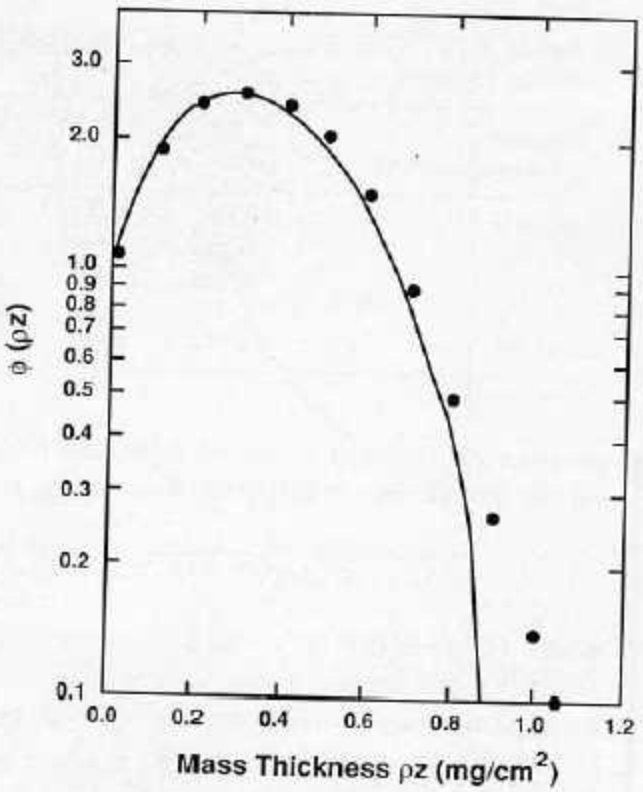

Figure 3.44. Depth distribution function $\phi(\rho z)$ of x rays produced in aluminum. Experimental data of Castaing and Henoc (1966), Monte Carlo calculation of Newbury and Yakowitz (1976).

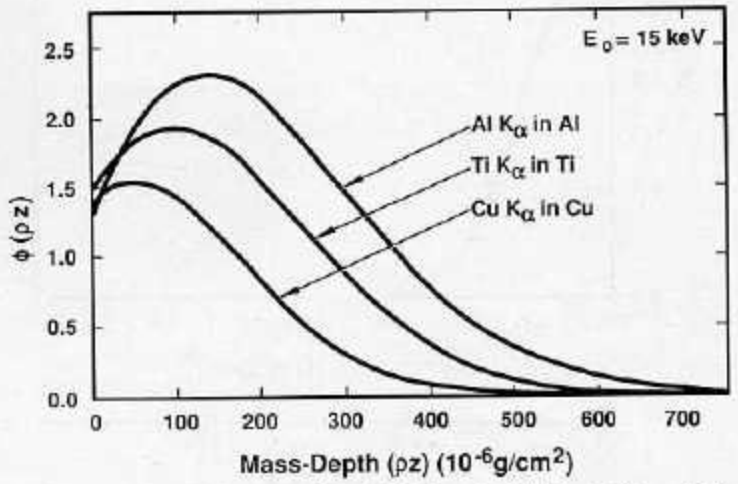

Figure 8.5. Calculated $\phi(\rho z)$ curves for Al $K\alpha$ in Al, Ti $K\alpha$ in Ti, and Cu $K\alpha$ in Cu at 15 keV.

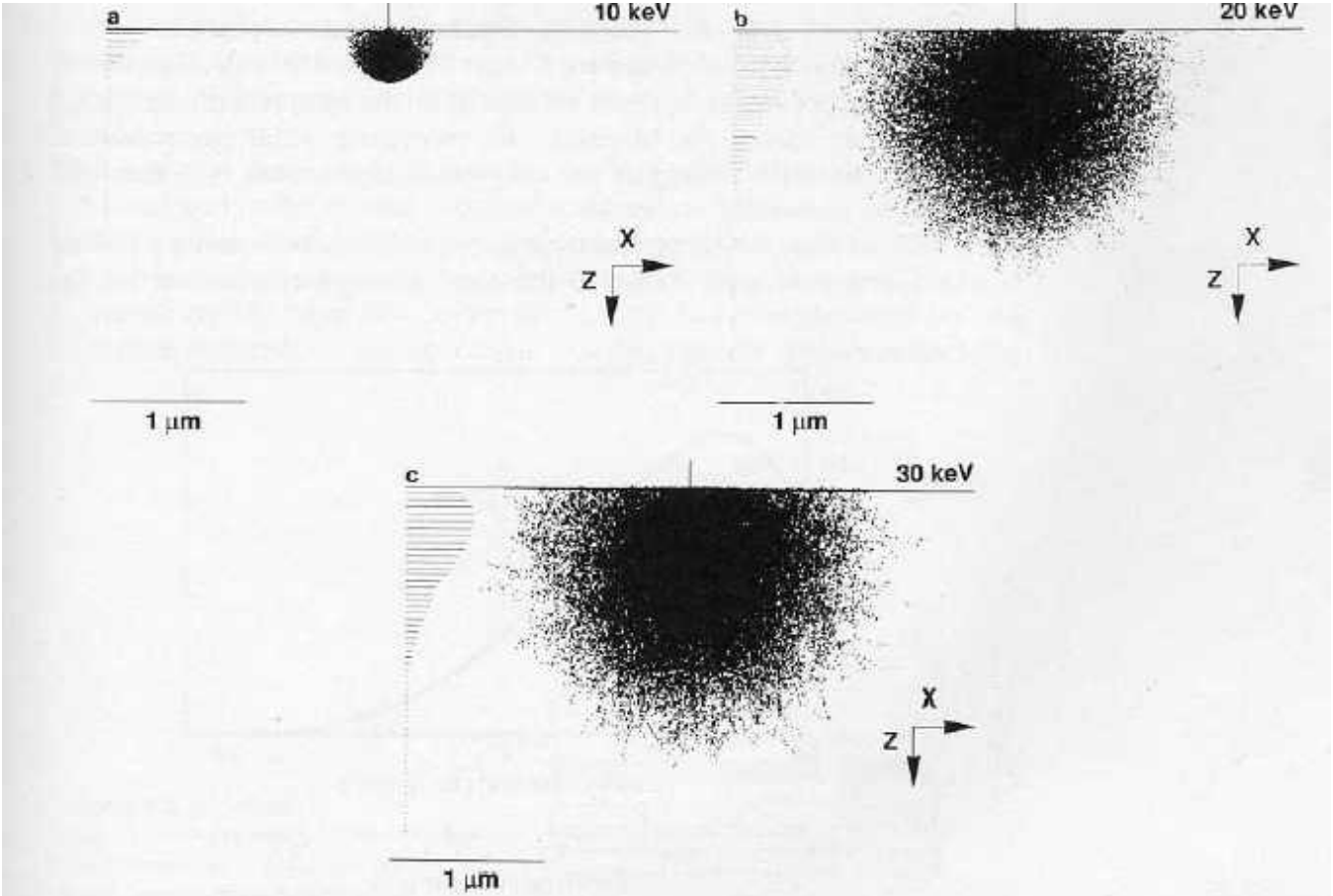

Figure 8.7. Monte Carlo calculations of x-ray generation volume for Cu at (a) 10, (b) 20, and (c) 30 keV.